CENTRO DE INVESTIGACIONES
EN OPTICA, A.C.

“DESIGN OF AN INTEGRATED PHOTON PAIR SOURCE BASED ON COUNTER-PROPAGATING SPONTANEOUS FOUR WAVE MIXING IN A Si_3N_4 MICRORING RESONATOR”

Tesis que para obtener el grado de Doctor en Ciencias (Óptica)

Presenta: Gerardo de Jesús Rodríguez Becerra

Director de Tesis: Dr. Roberto Ramírez Alarcón
Co – Director de Tesis: Dr. Rafael Salas Montiel

León · Guanajuato · México
Marzo de 2025

Design of an Integrated Photon Pair Source Based on Counter-Propagating Spontaneous Four Wave Mixing in a Si_3N_4 Microring Resonator

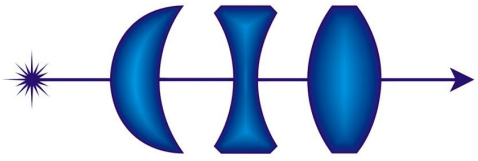

Gerardo de Jesús Rodriguez Becerra

Quantum Photonics Group

Centro de Investigaciones en Óptica A.C.

Submitted in Partial Fulfillment of the Requirements for the Degree of

Doctor of Science (Optics)

CIO March 2025

Dedicated to my parents, Jerónimo Rodríguez and Juana Becerra.

Declaration

I hereby declare that, except where explicit reference is made to the work of others, the content of this dissertation is original and has not been submitted, either in whole or in part, for consideration toward any other degree or qualification at this or any other university.

Gerardo de Jesús Rodriguez Becerra

March 2025

Acknowledgements

At last, I am writing this section to express my gratitude to the people I have been fortunate to meet throughout my PhD at CIO. Over these four years, they have each contributed to my journey in various personal and academic ways.

I am deeply grateful to my parents and siblings for their love and support.

I would like to express my sincere gratitude to my advisors, Dr. Roberto Ramírez Alarcón and Dr. Rafael Salas Montiel for their support and guidance along my entire PhD journey.

I would like to thank the professors who taught me during my time at CIO, especially Dr. Laura Rosales for allowing me to attend her quantum optics and quantum information courses, even though I was not formally enrolled in them.

Thank you to my thesis tutoral committee members: Dr. Alfredo Benitez, Dr. Carlos Wiechers, Dr. Lorena Velazquez, for their comments and suggestions. Your feedback was very helpful in the development of this work.

I sincerely thank my thesis examiners, Dr. Carlos Wiechers, Dr. Laura Rosales, and Dr. Verónica Vázquez, for taking the time to review my work and for their valuable corrections and suggestions.

Thank you to my academic tutor, Dr. Carmelo Rosales for his advices.

I would like to express my heartfelt gratitude to my research group partners and friends, with whom I spent most of my time at CIO. Our enriching conversations, both academic and beyond, deeply impacted me and shaped my perspective on the world. Thank you, Dante, Edwin, Guillermo, Paty Ornelas, Paty Tavares and Samuel.

I'm deeply grateful to those people who welcomed me into their extracurricular activities, especially the football team I played with over these years: Brandon, Cecilia, Dante, Edgar Reyes, El Mike, Dani Esparza, Chimi, Celedón, Daniel, and Pipe. Thank you all.

Thank you to Guillermo Aragón for organizing board game and video game sessions with the group. It was fun and a great way to relax.

I am grateful to CONAHCYT for the financial support provided over these four years.

Lastly, thank you to the programme ECOS Nord M19P01 of the University of Technology of Troyes.

Abstract

Photon sources based on parametric processes play an important role for the implementation of quantum protocols that use single photons as carriers of quantum information. These type of photon sources rely on heralding schemes, where the detection of one photon announces the presence of its twin. For these sources to function effectively, the photon pairs produced must be in a spectrally pure state. Otherwise, detecting one photon collapses its twin into a mixed state rather than a pure one, negatively impacting the performance. While spectral filtering after generation can purify the states, this approach significantly reduces the photon count rate. An alternative strategy is to tailor the spectral properties of the photon pairs through group velocity dispersion (GVD) engineering, a complex process that involves carefully tuning the waveguide's geometrical parameters to ensure the generated states are not spectrally entangled.

In this work, we present a novel design of a visible-telecom photon pair source based on Counter-Propagating Spontaneous Four Wave Mixing (CP-SFWM) within a silicon nitride microring resonator. We detail the design process, including the determination of geometrical parameters, and provide simulations of the source's emission rate and spectral properties. Our results demonstrate that utilizing a high-quality resonant cavity enables the generation of photon pairs in a spectrally pure state. Unlike conventional designs based on co-propagating SFWM, the proposed integrated source achieves automatic phase matching, eliminating the need for dispersion engineering and significantly simplifying the design process. Furthermore, we compare our approach to the original proposal of a photon source based on CP-SFWM in an optical fiber, showing that our design offers superior spectral characteristics, higher emission rate, and scalability. Finally, we present the spectral characterization of a ring resonator

fabricated in the University of Technology of Troyes, achieving quality factors sufficient to generate photon pairs in pure state. These results underscore the potential of the CP-SFWM approach as a promising alternative for integrated on-chip photon pair generation.

Table of contents

List of figures

List of tables

Chapter 1

Introduction

1.1 Preamble

Since its inception, quantum mechanics has disconcerted the scientific community with its seemingly counterintuitive predictions, particularly its probabilistic nature, which contrasted with the deterministic outcomes predicted by well-established theories, such as classical mechanics and electrodynamics. From the beginning, there was a group of scientists who argued that the probabilistic character and the "strange" predictions of the theory were due to its incompleteness [1, 2]. To date, numerous experiments have confirmed predictions of quantum mechanics [3–7], particularly following the invention of laser technology in 1960 [8]. This innovation, a coherent and high-intensity light source, opened the door to rapid advancements not only in nonlinear optics [9, 10] but also in quantum optics, as it enabled the generation of nonclassical states of light. Experiments using optical quantum states have demonstrated foundational effects in quantum theory [11–17], while also enabling the implementation of protocols based on quantum information encoded in photons, such as quantum key distribution [18, 19], quantum computing [20, 21], and quantum metrology [22, 23].

The implementation of these emerging quantum technologies relies on the production, detection, and manipulation of photonic quantum states. In this work, we focus on the problem of generating photon pairs in pure state, as many of the applications mentioned rely on single photons that are indistinguishable in all degrees of freedom.

1.2 Types of Single Photon Sources

An ideal single photon source, a so called photon gun, is one that emits a single photon at a specific time with tailored spectral properties suited to the application for which it was designed. Implementations of these sources fall into two categories: deterministic and probabilistic. Deterministic sources use two-level quantum systems, initially in the ground state, which are excited through electrical [24] or optical [25] methods to a higher energy level; they emit a photon as the system returns to the ground state. Examples include quantum dots [25, 26] and single atoms [27]. These approaches have certain drawbacks, such as requiring challenging operating conditions, such as high-vacuum environments and cryogenic temperatures, and emitting photons in random directions, which necessitates additional design to direct the emission [28]. The second alternative, known as probabilistic sources, involves generating photon pairs through nonlinear parametric processes such as spontaneous parametric down-conversion (SPDC) and spontaneous four-wave mixing (SFWM). SPDC is a process in which a single pump photon is converted into two lower-energy photons through a nonlinear interaction in a material with second-order nonlinear susceptibility ($\chi^{(2)}$). For the generation via SFWM two pump photons are involved, which do not necessarily have the same energy. This interaction occurs in a third-order nonlinear medium ($\chi^{(3)}$). An important difference of photon-pair generation using these processes is that SPDC is typically implemented on materials in bulk, whereas SFWM can be implemented in optical fibers or waveguides. In Figure 1.1, we show the energy level diagrams of these two processes.

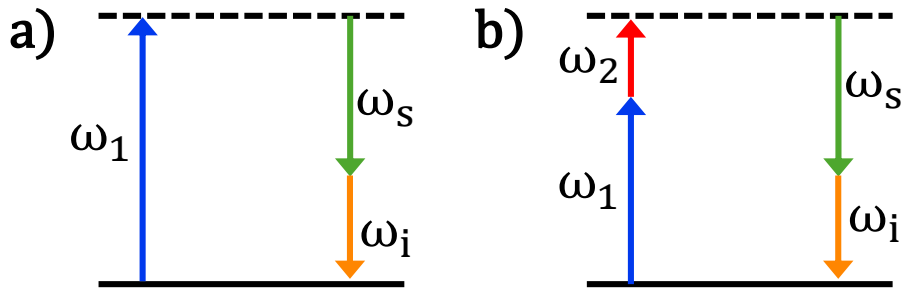

Fig. 1.1 Energy diagrams represent graphically the energy conservation in nonlinear parametric processes, which is satisfied along with phase matching. These conditions are expressed respectively for SPDC and SFWM as a) $\omega_1 = \omega_s + \omega_i$, $\mathbf{k}_1 = \mathbf{k}_s + \mathbf{k}_i$ and b) $\omega_1 + \omega_2 = \omega_s + \omega_i$, $\mathbf{k}_1 + \mathbf{k}_2 = \mathbf{k}_s + \mathbf{k}_i$. Subscripts denote pumps one and two, signal and idler.

Probabilistic photon sources are effectively used in quantum protocols using a so-called heralding scheme. This consists on detecting one photon of the pair, which signals the existence of its twin created during the parametric process. This scheme is illustrated in Figure 1.2.

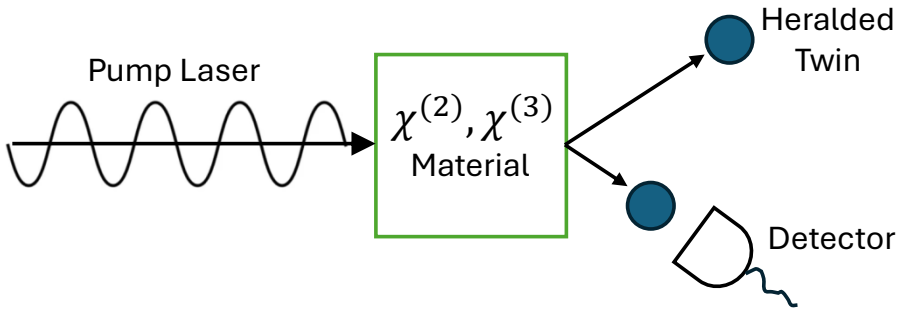

Fig. 1.2 Basic concept of a single photon source based on a parametric nonlinear process.

An important requirement for these photons to be useful in the implementation of quantum protocols is that the quantum state describing the pair must be unentangled in all degrees of freedom. In a single-photon heralding scheme, any entanglement would cause the detection of the herald photon to project its twin into a mixed state rather than a pure one. This loss of purity makes the photons distinguishable, which can degrade the performance of the applications relying on them, as the photonic states are not consistently prepared under identical conditions. When the pair is in an unentangled state, detecting the herald photon only provides information about the existence of its twin, preserving its indistinguishable nature.

Photon sources based on SFWM in various types of optical fibers [29–33] have gained attention in recent years due to interesting properties, such as an emission rate that scales quadratically with pump power [34], and the flexibility to adjust the interaction length as needed. However, photon pairs generated through parametric nonlinear processes are inherently subject to spectral entanglement due to energy and momentum conservation. The primary approach to address this issue is to filter spectrally the photons [35], but this leads to a reduction of the photon-pair production rate, an important feature for the efficient implementation of quantum protocols. An alternative solution, known as group velocity matching (GVM) engineering [36–39], involves tuning the parameters of the photon source so that the Joint Spectral Intensity (JSI) function of the generated photons is separable, a requirement for achieving heralded single photon states.

1.3 Chip Integrated Single Photon Sources

Similar to advancements in electronic technology, progress in optical applications follows the trend of transitioning from laboratory-based implementations to compact, integrated devices suited for use outside of laboratory environments. In recent years, integrated photon sources on quantum photonic chips have gained significant attention [40–46] since this platform offers promising features, including room-temperature operation, low decoherence, flexible geometric designs that can be tailored for specific applications, and compatibility with production using CMOS manufacturing technology [47]. To mention some reported fully integrated applications on chip, examples include boson sampling [48] and quantum teleportation [49].

Some implementations of integrated photon sources are based on waveguides in straight [50, 51] or spiral [52, 53] geometries, but they have the drawback that waveguides must be of several centimeters to produce considerable amount of photon pairs and this would affect its scalability in applications on chip. An interesting scheme are sources based on resonant cavities which solve this problem as the enhanced cavity lifetime makes possible to produce a

high photon rate with low pump power in a micrometric device. Another interesting property of photon pairs produced in resonant cavities is that bandwidth of photons can be significantly reduced using a high quality cavity [54]. This makes this kind of sources viable for applications in which atom-light interactions are needed, such as optical quantum memories. In these protocols, photons with a precise wavelength and narrow bandwidth are essential to excite specific atomic transitions, a key factor for efficient performance [55–57]. Photon sources based on microring resonators have been successfully used in quantum applications, including quantum teleportation [58], boson sampling [59], quantum key distribution (QKD) [60, 61], frequency comb generation [62, 63], quantum computing gates [64], and Franson interferometry [46, 65].

1.4 Motivation

In [66], the authors proposed the Counter-Propagating SFWM (CP-SFWM) scheme, in which two pump lasers are injected from opposite ends of an optical fiber. This scheme exhibits interesting properties; for example, the energy and phase-matching conditions are directly satisfied for photon emissions at the same wavelengths as the pump lasers but in opposite directions, simplifying the design by eliminating the need to fine tune the fiber parameters to position a zero-dispersion point near the pump wavelength. Additionally, they showed that this setup enables the generation of photons in a pure state using an optical fiber sufficiently long.

In recent years, several studies have theoretically investigated [67–69] and experimentally demonstrated [70–72] the generation of photon pairs via SPDC and SFWM in counter-propagating configurations. Experimental implementations have confirmed the advantages of these schemes, including easy tunability, narrow bandwidths, and spectral separability. The latter is particularly crucial for Hong-Ou-Mandel interference with photons from different sources, which is fundamental to scalable photonic quantum computing [21].

These properties of counter-propagating schemes, demonstrated in bulk and optical fibers, motivated this thesis, in which we investigate the features of a cavity-enhanced integrated photon source based on CP-SFWM. We demonstrate that a photon source implemented with this scheme, even with a relatively low quality factor ($Q \sim 10^4$), can easily overcome the complex group velocity engineering process [36–39] required to ensure spectral separability in the co-propagating scheme.

Additionally, compared to cavity-enhanced photon sources based on co-propagating SFWM, our CP-SFWM source offers significant advantages due to its automatic phase-matching mechanism. Specifically, it eliminates the need for precise tuning of the waveguide cross-section to satisfy phase-matching conditions at the target wavelengths. Furthermore, it does not require dispersion engineering to position the zero-dispersion point near the pump wavelength in the anomalous dispersion region. Simultaneously satisfying both conditions is challenging, as they are highly sensitive to geometric variations and require precise control over the waveguide dimensions [73, 74]. Another advantage of our photon source is its operation with only two wavelengths, whereas the co-propagating scheme requires three. The latter necessitates tuning the ring radius to achieve three resonant wavelengths, complicating both the design and operation.

This enhanced simplicity and flexibility make our scheme highly adaptable to a wide range of applications, requiring only lasers operating at the desired wavelengths and compatible detectors. Such versatility establishes our approach as a robust framework for designing tailored integrated photon-pair sources. Notably, it presents an especially attractive solution for applications such as integrated solid-state quantum memories based on rare-earth ions, where generating photons with precise wavelengths and narrow bandwidths is crucial for efficient light-matter interaction. This further underscores the significance of our approach.

1.5 Thesis Outline

The content of this thesis is divided in five chapters, the first one being this introduction. In chapter two we present the design considerations of the integrated photon source, a review on the materials, and a brief discussion on the theory of guided modes and the quantization of electromagnetic field. In chapter three we make the explicit full derivation of the quantum state of photon pairs using the CP-SFWM scheme in a resonant ring cavity. We include a section dedicated to the Schmidt decomposition, a technique used to quantify the degree of entanglement in a bipartite system, and we compute the expression for the emission rate of photon pairs by our source. In chapter four we present the results obtained in the simulations using parameters of materials and equipment we have in our facilities, with which we selected the appropriate parameters of the photon source, and then we analyze the spectral properties and emission rate, and make a comparison with the original proposal using an optical fiber [66]. Additionally, we present the spectral characterization of a ring resonator fabricated in the University of Technology of Troyes. Finally, in chapter five we present the conclusions.

Chapter 2

Design Considerations of the Photon Source and Fundamentals

2.1 Spontaneous Four-Wave Mixing Processes

Spontaneous Four-Wave Mixing is a nonlinear process that occurs in materials with a third-order nonlinear susceptibility ($\chi^{(3)}$). It is typically implemented in optical fibers or waveguides. The term spontaneous distinguishes this process from its stimulated counterpart, where, in addition to the pump lasers, an extra laser is injected into the fiber or waveguide. This additional laser seeds the FWM process, enhancing its efficiency. However, the generated photons cannot be used in quantum technology applications, as they mix with the stimulating laser photons. In the spontaneous case, only the pump laser is injected into the fiber or waveguide, leading to the generation of signal-idler photon pairs through a quantum interaction. Figure 2.1 illustrates a diagram of a photon-pair source implemented in an optical fiber using the co-propagating method, so named because the generated photons propagate in the same direction as the pump field. We focus on the pump-degenerate case, where a single pump laser is used, meaning both pump photons have the same frequency.

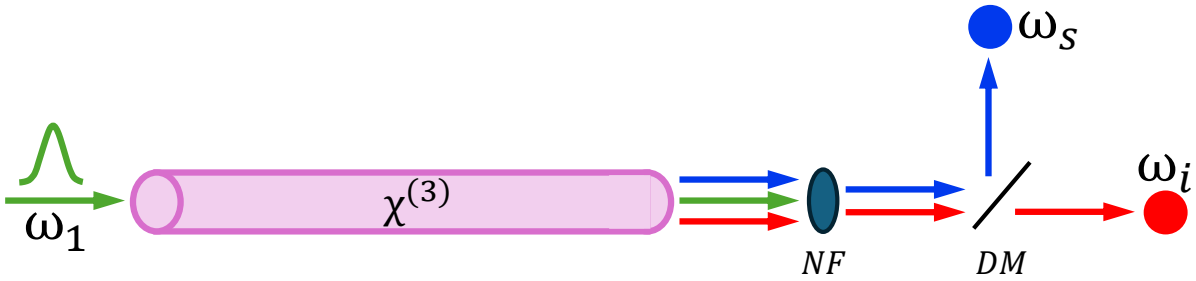

Fig. 2.1 Diagram of co-propagating SFWM. In this configuration, the signal and idler photons are generated in the same direction as the pump field. At the output of the fiber, the remaining pump laser can be removed using a Notch filter (NF), while the signal and idler photons can be separated using a dichroic mirror (DM).

In the relevant work [66], J. Monroy-Ruz and colleagues proposed the Counter-Propagating Spontaneous Four-Wave Mixing (CP-SFWM) scheme, an alternative approach to the typical co-propagating single pump SFWM scheme to generating heralded photon pairs that are tunable, bright, factorable, and exhibit narrow bandwidths. This method, illustrated in Figure 2.2 a), involves coupling two laser beams into opposite ends of a $\chi^{(3)}$ nonlinear waveguide or optical fiber.

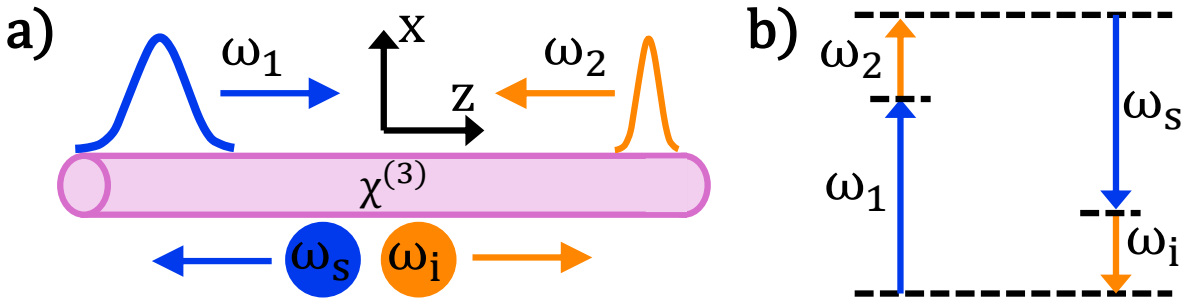

Fig. 2.2 a) Schematic of the CP-SFWM process in a $\chi^{(3)}$ waveguide, pumps 1 and 2 are depicted by Gaussian shapes while the photons generated in the process are represented by the bottom spheres. The arrows indicate the direction of propagation. b) Energy level diagram for CP-SFWM, the energy conservation is trivially satisfied for $\omega_s = \omega_1$ and $\omega_i = \omega_2$.

For the counter-propagating setup, the phase-matching condition is automatically satisfied for $\omega_s = \omega_1$, and $\omega_i = \omega_2$, while energy conservation dictates $\omega_1 + \omega_2 = \omega_s + \omega_i$ as depicted in Figure 2.2 b). During the process, pump photons at frequencies ω_1 and ω_2 interact in the

nonlinear material creating a new photon pair that matches the pump wavelengths but propagate in opposite directions. This bidirectional setup not only simplifies the tuning of the output photon wavelengths but also enhances experimental flexibility. An important concept in the design of waveguides is the dispersion [75], defined as

$$D(\lambda) = -\frac{\lambda}{c}\frac{d^2 n_{eff}(\lambda)}{d\lambda^2}, \tag{2.1}$$

where c is the speed of light in vacuum, $n_{eff}(\lambda)$ is the effective refractive index of the guided mode, and λ is the wavelength. In photon sources based on the co-propagating SFWM scheme, dispersion must be carefully evaluated, as the pump wavelengths must be confined to the anomalous dispersion regime near a zero-dispersion point [73, 74]. The CP-SFWM has the advantage of its inherent phase-matching, eliminating the need for dispersion engineering. This relaxed constraint simplifies the design process, requiring only that the waveguide supports guided modes at the pump frequencies. Additionally, this configuration broadens the applicability of CP-SFWM to a wider range of materials and wavelength regimes, further emphasizing its versatility and potential for practical implementations.

In their work, Monroy-Ruz and colleagues explored two configurations of CP-SFWM in an optical fiber. They demonstrated that using a combination of a continuous wave (CW) laser and a pulsed laser as pumps, referred as the mixed case, offers several advantages. Specifically, this approach allows for a simultaneous increase in photon emission rate, the generation of factorable quantum states, and a reduction in photon bandwidth as the interaction length grows. While their findings showed that optical fibers only a few millimeters long could generate spectrally separable photon pairs, achieving photon bandwidths in the MHz range required optical fibers or waveguides several meters long. Such dimensions suppose significant challenges for scalability, particularly in the context of photonic integrated circuits (PICs) and key applications in quantum networks, such as integrated quantum memory devices. To overcome this limitation, we propose a novel approach that implements CP-SFWM within a high-quality integrated microring resonator fabricated on the silicon nitride (Si_3N_4) platform.

We will explain in Chapter 4 that the radius of the ring cavity must be carefully chosen through an optimization method aimed at ensuring that the signal–pump 1 and idler–pump 2 beams are resonant. In other words, the challenge is to optimize two resonances. This represents a simplification compared to the co-propagating SFWM scheme, where the optimization process involves three resonances, one for each field: pump, signal, and idler.

2.2 Configuration of the Photon Source

The photon pair source proposed in this work features a silicon nitride-on-insulator microring resonator in an add-drop configuration, as illustrated in Figure 2.3 a). The design is based on ridge type waveguides, shown in Figure 2.3 b).

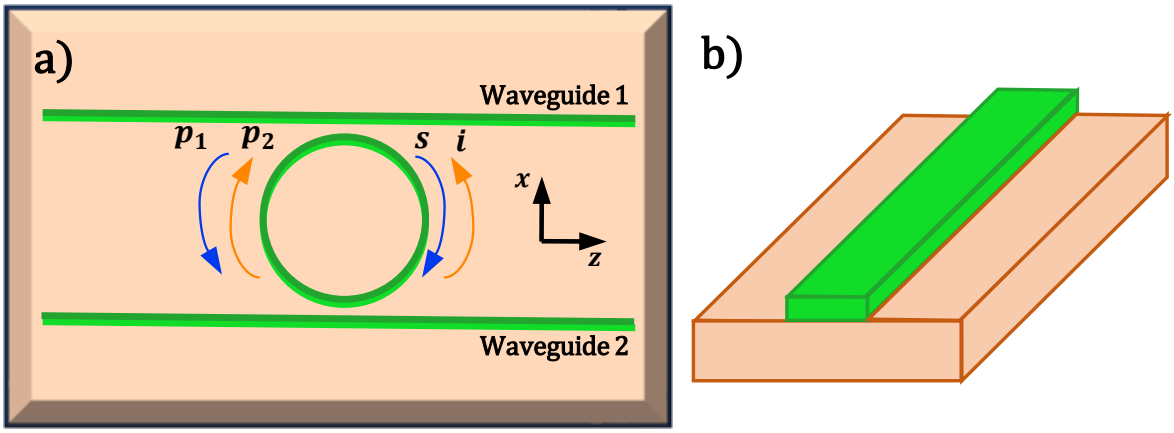

Fig. 2.3 a) Schematic of the proposed photon pair source. Waveguide 1 works as input port for pump 1 and at the same time as drop port for signal photons, waveguide 2 has the same function but for pump 2 and idler photons. b) Schematic of a ridge type waveguide.

Four key parameters must be considered in the design: the height and width of the waveguides, the radius of the ring resonator cavity, and the gaps between the ring and the bus waveguides. In Chapter 3, we present a comprehensive analysis of the microring-based photon source, detailing its design and performance characteristics. In Chapter 4, we provide a detailed

explanation of the criteria and methods used to select these parameters with the objective to optimize the performance of the photon source.

2.3 Properties of Silicon Nitride

Silicon-on-Insulator (SOI) is a versatile material that has been widely utilized in integrated photonics research [76] due to its availability and properties. Its high refractive index [77] allows for the dense integration of components on a single chip, while its compatibility with CMOS technology [78] enables efficient large-scale fabrication. However, SOI has certain drawbacks. For instance, it is not transparent at visible wavelengths [79], limiting its applications in this spectral range. Moreover, its low bandgap negatively impacts photon-pair generation via spontaneous four-wave mixing due to undesired effects such as two-photon absorption (TPA) and free-carrier absorption (FCA) [80, 81].

In recent years, alternative materials have been explored. One prominent example is silicon nitride (Si_3N_4), which we use in our design. While its refractive index, as well as linear and nonlinear properties, are slightly lower than those of SOI [82], it offers significant advantages. Its higher bandgap eliminates TPA and FCA [83], and its wide transparency window includes visible wavelengths [84, 79] expanding its range of applications. Furthermore, silicon nitride exhibits an exceptionally low loss coefficient [85, 86], which is critical for developing high-quality resonant cavities that enhance photon-pair production [87]. Silicon nitride has been successfully employed in various on-chip applications, including photon-pair sources operating across visible and telecom wavelength ranges [46, 88–90], phase modulators [91, 92], chip-integrated lasers [93, 94], sensors [95, 96], and optical filters [97]. In table 2.1, we summarize the properties of both materials.

	SOI	Si_3N_4
Transparency window (μm)	1.1-8	0.4-7
Refractive index	3.5	2
Nonlinear refractive index (m^2/W)	4×10^{-18}	3.1×10^{-19}
Bandgap (eV)	1.12	5.3
loss coefficient (dB/cm)	~ 2 [98, 99]	0.001

Table 2.1 Relevant properties of *SOI* and Si_3N_4 for the development of photon pair sources.

2.4 Theory of Guided Modes

A common misconception about guiding of light in optical fibers and waveguides is the assumption that this phenomenon is entirely explained by total internal reflection. Total internal reflection plays a role, but this explanation is overly simplified. If it were the complete explanation, we would observe a continuum of guided modes, all satisfying the critical angle condition, which is not observed in experimental results [100]. A good understanding of the guiding effect can be obtained by solving the step-index optical fiber using a wave optics approach [101]. The profile of a step-index optical fiber is depicted in Figure 2.4.

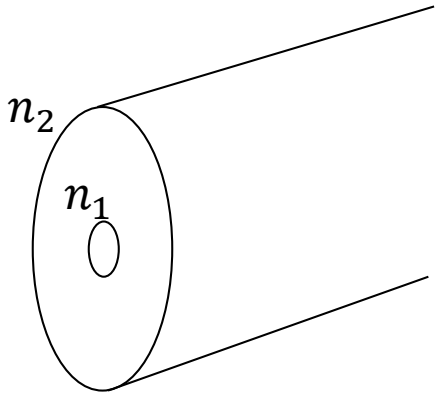

Fig. 2.4 Graphical representation of a step-index optical fiber. It exhibits radial symmetry. n_1 and n_2 are the refractive index of core and cladding, respectively.

This type of optical fiber consists of a core with refractive index n_1, and a cladding with n_2, for which the condition $n_1 > n_2$ is satisfied. The analysis begins with the wave equation of the electric field in a dielectric media, expressed as

$$\nabla^2 \boldsymbol{E}(\boldsymbol{r},t) - \frac{n(r)^2}{c^2}\frac{\partial \boldsymbol{E}(\boldsymbol{r},t)}{\partial t} = 0. \tag{2.2}$$

where $n(r)$ is the refractive index function, and c is the speed of light. The first step is to separate the temporal dependence from the spatial one, then a trial solution of the form $\boldsymbol{E}(\boldsymbol{r},t) = \boldsymbol{E}(\boldsymbol{r})e^{-i\omega t}$ is used. Substituting this into the wave equation and expressing the Laplacian operator in cylindrical coordinates, equation (2.2) rewrites as

$$\left(\frac{\partial^2}{\partial r^2} + \frac{1}{r}\frac{\partial}{\partial r} + \frac{1}{r^2}\frac{\partial}{\partial \phi} + \frac{\partial^2}{\partial z^2} + \beta^2\right)\boldsymbol{E}(\boldsymbol{r}) = 0 \tag{2.3}$$

where $\beta = \frac{n\omega}{c}$ is the wave number in the medium and ω is the angular frequency. To solve the spatial part, a trial solution is proposed: $\boldsymbol{E}(\boldsymbol{r}) = E(r)e^{i(l\phi+\beta z)}$, where β is the effective wave number of the wave traveling along z. Substituting this into equation (2.3) reduces it to an ordinary differential equation in r.

$$\frac{d^2E(r)}{dr^2} + \frac{1}{r}\frac{dE(r)}{dr} + \left(n^2(r)k^2 - \beta^2 - \frac{l^2}{r^2}\right) = 0 \tag{2.4}$$

This is a well-known Bessel differential equation. To ensure physically meaningful solutions, this is, no singularities in the core, convergence to zero in the cladding, and continuity and smoothness at the core-cladding interface, the azimuthal dependence must be periodic. This condition requires the parameter l to be an integer. All these requirements define the guided modes in the optical fiber, which are given by Bessel functions of first kind ($J(r)$) in the core and of second kind ($Y(r)$) in the cladding.

Figure 2.5 a) shows the transverse field distribution for a step-index optical fiber, simulated using Metric software [102] with typical values for the core-radius and refractive indices. In Figure 2.5 b), it is appreciated that the field distribution extends outside the core, an effect not accounted for in the simplified geometrical optics description. This phenomenon, known as the evanescent field, plays a crucial role in the development of integrated photonic circuits.

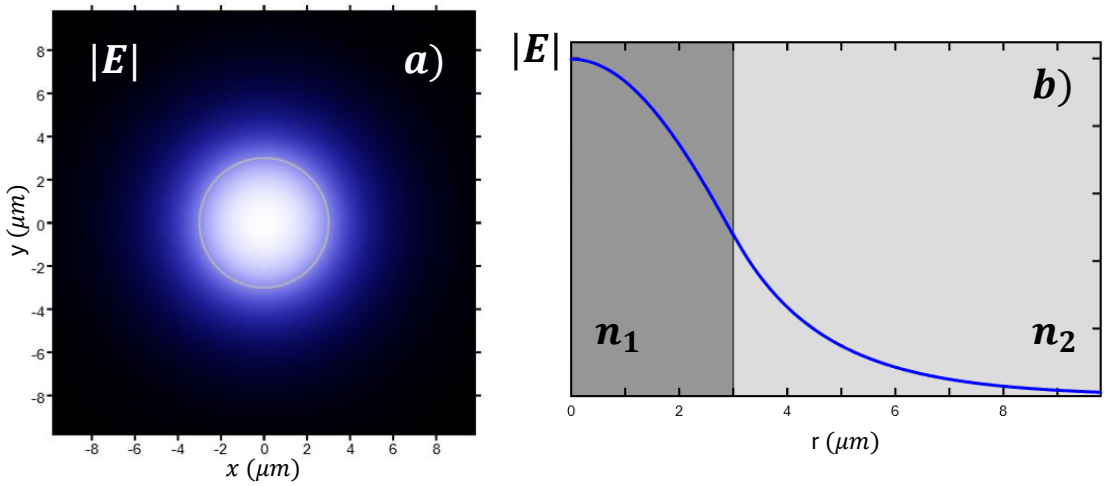

Fig. 2.5 Field distribution of the fundamental mode in a step-index optical fiber. The parameters used in the simulation are $n_1 = 1.5$, $n_2 = 1.49$, $\lambda = 1550\,nm$, $R_{core} = 3\,\mu m$. a) Normalized transverse field distribution. b) Normalized profile as function of r.

For optical fibers with more complex refractive index profiles or waveguides with structures such as rectangular profiles and several cladding materials, like the one considered in this work, it is not possible to solve the transverse field distribution analytically. Instead, it is necessary to use numerical methods or specialized software [103].

2.5 Quantization of the Electromagnetic Field

In this section, we provide a concise overview of the quantization of the electromagnetic field and Fock states. The description of spontaneous four wave mixing cannot be fully explained within the framework of classical electrodynamics, therefore a quantum mechanical treatment is necessary. In classical reference textbooks we can find the quantization procedure for a set of standing waves in 3D free space [104, 105]. Here we focus on the analysis for the case of a 1D cavity of length L_Q (which ultimately in the analysis of the photon source will be considered $L_Q \to \infty$) with perfect reflective walls, assuming there are nor currents nor charges.

The electric and magnetic fields can be expressed in terms of the vector potential $\boldsymbol{A}(\boldsymbol{r},t)$, as follows

$$\boldsymbol{E}(\boldsymbol{r},t) = -\frac{\partial \boldsymbol{A}(\boldsymbol{r},t)}{\partial t}, \tag{2.5}$$

$$\boldsymbol{B}(\boldsymbol{r},t) = \boldsymbol{\nabla} \times \boldsymbol{A}(\boldsymbol{r},t), \tag{2.6}$$

The Coulomb gauge is imposed, $\boldsymbol{\nabla} \cdot \boldsymbol{A} = 0$, to ensure the electrical and magnetic field components of the radiation are both transversal to the propagation vector. With this consideration, a wave equation for the vector potential can be derived from the Maxwell equations

$$\boldsymbol{\nabla}^2 \boldsymbol{A}(\boldsymbol{r},t) - \frac{1}{c^2}\frac{\partial \boldsymbol{A}(\boldsymbol{r},t)}{\partial t} = 0. \tag{2.7}$$

The solution is a superposition of harmonic waves linearly polarized along $\hat{\boldsymbol{x}}$, all satisfying the standing wave condition, $\lambda = L_Q/m$, $k = 2\pi m/L_Q$, with $m = 1,2,3,...$

$$\boldsymbol{A}(\boldsymbol{r},t) = \hat{\boldsymbol{x}} \sum_k \left[A_k e^{i(kz-\omega t)} + A_k^* e^{-i(kz-\omega t)} \right], \tag{2.8}$$

where A_k denotes the complex amplitude of the field. The quantized electric and magnetic fields, written in terms of annihilation and creation operators are given by [105]

$$\hat{\boldsymbol{E}}(\boldsymbol{r},t) = i\hat{\boldsymbol{x}} \sum_k \left(\frac{\hbar \omega_k}{2\varepsilon_0 V} \right)^{1/2} \left[\hat{a}_k e^{i(kz-\omega_k t)} - \hat{a}_k^\dagger e^{-i(kz-\omega_k t)} \right] \tag{2.9}$$

$$\hat{\boldsymbol{B}}(\boldsymbol{r},t) = \frac{i}{c}\hat{\boldsymbol{y}} \sum_k \left(\frac{\hbar \omega_k}{2\varepsilon_0 V} \right)^{1/2} \left[\hat{a}_k e^{i(kz-\omega_k t)} - \hat{a}_k^\dagger e^{-i(kz-\omega_k t)} \right] \tag{2.10}$$

Where ε_0 is the electric permittivity of vacuum, and V is the volume of interaction. At this point we introduce some modifications to adapt the equation of the quantized electromagnetic field to describe the guided field within a waveguide. The vacuum wave number is replaced by the propagation constant associated with the guided mode, β. Since the electromagnetic radiation propagates in a dielectric medium, we also made the substitution $\varepsilon_0 \rightarrow \varepsilon_0 n_{eff}^2(\beta)$, where $n_{eff}(\beta)$ is the effective refractive index of the guided mode. Furthermore, as the radiation

travels only along the z-axis, the spatial volume is defined by the cavity length, L_Q, and the spatial density of the guided mode, $f(x,y)$, which is normalized $\int\int f_\beta^2(x,y)dxdy = 1\ m^{-1}$. From now on, we focus on the electric field as the SFWM treatment is conducted using this field. With these adjustments, equation (2.9) becomes

$$\hat{\boldsymbol{E}}(\boldsymbol{r},t) = i\hat{\boldsymbol{x}}\sum_\beta \left(\frac{\hbar\omega_\beta}{2\varepsilon_0 n_{eff}^2(\beta)L}\right)^{1/2} f_\beta(x,y)\left[\hat{a}_\beta e^{i(\beta z-\omega_k t)} - \hat{a}_\beta^\dagger e^{-i(\beta z-\omega_k t)}\right] \tag{2.11}$$

Finally, we define the mode spacing in terms of the quantization length, L_Q, as

$$\delta k = 2\pi/L_Q, \tag{2.12}$$

and define the common factor of the sum as

$$\ell(\beta) = \sqrt{\frac{\hbar\omega_\beta}{\varepsilon_0 n_{eff}^2(\beta)}} \tag{2.13}$$

Incorporating definitions (2.12,2.13), the quantized electric field can be expressed as

$$\hat{\boldsymbol{E}}(z,t) = i\frac{\sqrt{\delta k}}{2}\hat{\boldsymbol{x}}\sum_\beta \ell(\beta) f_\beta(x,y)\left[\hat{a}_\beta e^{i(\beta z-\omega_k t)} - \hat{a}_\beta^\dagger e^{-i(\beta z-\omega_k t)}\right] \tag{2.14}$$

Now we present the Fock states. The annihilation and creation operators appearing in (2.14) satisfy the following commutation relations

$$\begin{aligned}\left[\hat{a}_\beta, \hat{a}_{\beta'}\right] &= 0\\ [\hat{a}_\beta^\dagger, \hat{a}_{\beta'}^\dagger] &= 0\\ [\hat{a}_\beta, \hat{a}_{\beta'}^\dagger] &= \delta_{\beta\beta'}\end{aligned} \tag{2.15}$$

The Hamiltonian of the electromagnetic modes inside the cavity can be expressed in terms of these operators as [105]

$$\hat{H} = \sum_{\beta} \hbar\omega_{\beta} \left(\hat{a}^{\dagger}_{\beta} \hat{a}_{\beta} - \frac{1}{2} \right) = \sum_{\beta} \hbar\omega_{\beta} \left(\hat{n}_{\beta} - \frac{1}{2} \right) \tag{2.16}$$

where $\hat{n}_{\beta} \equiv \hat{a}^{\dagger}_{\beta} \hat{a}_{\beta}$ is the number operator associated with mode β. The Fock states, represent states with a well defined number of photons in each mode, are eigenstates of both the Hamiltonian and the number operator. These states are denoted as

$$|\{n_j\}\rangle = |n_1, n_2, n_3, ...\rangle \tag{2.17}$$

where we used an enumerated representation for simplicity. In this expression, n_j denotes the number of photons in the j-th mode. The eigenvalues of the number operator and the Hamiltonian are given by:

$$\left(\sum_j \hat{n}_j \right) |\{n_j\}\rangle = \left(\sum_j n_j \right) |\{n_j\}\rangle \tag{2.18}$$

$$\hat{H} |\{n_j\}\rangle = \left(\sum_j \hbar\omega_j \left(n_j + \frac{1}{2} \right) \right) |\{n_j\}\rangle \tag{2.19}$$

Throughout this work we will use the notation $|n\rangle_{\beta}$ to represent a state with n photons in the mode β and zero in all the others. Then, the creation and annihilation operators acting on a photon in mode β are respectively:

$$\hat{a}^{\dagger}_{\beta} |n\rangle_{\beta} = \sqrt{n+1} \, |n+1\rangle_{\beta} \tag{2.20}$$

$$\hat{a}_{\beta} |n\rangle_{\beta} = \sqrt{n} \, |n-1\rangle_{\beta} \tag{2.21}$$

Chapter 3

CP-SFWM in a Resonant Ring Cavity

In this chapter, we derive the photon state generated by CP-SFWM in a ring resonator from first principles. We follow the procedure presented in [34, 87], where the authors derived the photon state for the case of co-propagating SFWM. As we explain in equation (3.8), in this work, we analyze the term $E_{1+}^{(+)}E_{2-}^{(+)}E_{s-}^{(-)}E_{i+}^{(-)}$ from the general case of a third-order nonlinear interaction, corresponding to CP-SFWM, whereas they work with the term $E_{1+}^{(+)}E_{1+}^{(+)}E_{s+}^{(-)}E_{i+}^{(-)}$. In the final expressions, we include all laser parameters rather than making approximations based on bandwidths. We begin by writing the Hamiltonian of the process, followed by the derivation of the photon state in a straight waveguide. Next, we present the interaction of radiation at the ring-bus waveguide interface, which gives rise to Airy functions. These functions are then incorporated into the Joint Spectral Intensity (JSI) of the process. Finally, we provide a brief overview of the Schmidt decomposition, a technique used to quantify the degree of entanglement in a bipartite system, and conclude by calculating the photon emission rate.

3.1 Hamiltonian of CP-SFWM in a Straight Waveguide

The derivation of the Hamiltonian for the CP-SFWM process begins with the expression for the energy of a classical pump field in a waveguide [106]

$$H = \frac{1}{2}\int_V \boldsymbol{E}\cdot\boldsymbol{D}\, dV, \tag{3.1}$$

where $\boldsymbol{E}$ and $\boldsymbol{D}$ represent the electric and displacement fields, respectively, and V is the interaction volume. The electric displacement field is given by [106]

$$\boldsymbol{D} = \varepsilon_0\boldsymbol{E} + \boldsymbol{P}, \tag{3.2}$$

where ε_0 is the permittivity of free space, and $\boldsymbol{P}$ is the polarization (the dipole moment per unit volume). This quantity models the interaction between electromagnetic fields and matter, and it can be written as a power series of the electric field amplitudes [107]

$$\boldsymbol{P}(t) = \varepsilon_0\left[\boldsymbol{\chi}^{(1)}\boldsymbol{E}(t) + \boldsymbol{\chi}^{(2)}\boldsymbol{E}^2(t) + \boldsymbol{\chi}^{(3)}\boldsymbol{E}^3(t) + \cdots\right], \tag{3.3}$$

where $\boldsymbol{\chi}^{(1)}$, $\boldsymbol{\chi}^{(2)}$, $\boldsymbol{\chi}^{(3)}$, ..., are the susceptibility tensors that determine the material's response to the electric field. The first term corresponds to linear effects, which are independent of the field intensity, while the higher-order terms represent nonlinear interactions of second, third, and higher orders. The second-order term is ignored because it vanishes in centrosymmetric media such as silicon nitride. The third-order term is the lowest-order nonlinear contribution in this material and is responsible for the spontaneous four wave mixing effect [107].

In the analysis, we consider that all involved fields are co-polarized along $\hat{x}$. Thus, $\boldsymbol{E}\cdot\boldsymbol{D}$ can be expressed as:

$$\boldsymbol{E}\cdot\boldsymbol{D} = \varepsilon_0\left(1+\chi^{(1)}\right)EE + \varepsilon_0\chi^{(3)}EEEE \tag{3.4}$$

The first term corresponds to linear effects, which we ignore since our interest lies in the dynamics of the third-order nonlinear terms responsible for the SFWM effect. Note that we use scalar expressions because all fields are assumed to be co-polarized. In this expression, $\chi^{(3)}$ represents the element $\chi^{(3)}_{xxxx}$ of the third-order nonlinear susceptibility tensor.

Another consideration is that the guided modes propagate along the z-axis. Modes traveling in the positive and negative directions can be written in complex form as follows [107]

$$E_+ = \frac{1}{2}\left[Ee^{i(\beta z-\omega t)} + Ee^{-i(\beta z-\omega t)}\right] = \frac{1}{2}\left[E_+^{(+)} + E_+^{(-)}\right] \tag{3.5}$$

$$E_- = \frac{1}{2}\left[Ee^{i(-\beta z-\omega t)} + Ee^{-i(-\beta z-\omega t)}\right] = \frac{1}{2}\left[E_-^{(+)} + E_-^{(-)}\right] \tag{3.6}$$

Here, E is the field amplitude, and β denotes the wave number of the mode. The second term in each equation can be interpreted as waves of "negative" frequency propagating in the opposite direction. The total field of four components can be expressed as:

$$E = E_1 + E_2 + E_i + E_s, \tag{3.7}$$

where the subscripts 1, 2, s, and i refer to pump 1, pump 2, signal, and idler, respectively. Substituting (3.7) into the nonlinear term of (3.4) using (3.5) and (3.6) for each field, we obtain all the third-order nonlinear interactions between the four fields. The interaction of our interest is the non-degenerate CP-SFWM process, specifically the term of the form

$$E_{1+}^{(+)} E_{2-}^{(+)} E_{s-}^{(-)} E_{i+}^{(-)} \tag{3.8}$$

In this interaction, positive frequency terms are used for the pump fields, and negative frequency terms are used for the signal and idler fields, as this choice ensures energy conservation. Then, negative frequencies can be interpreted as fields created during the interaction.

Performing the algebra, and considering that the factors commute, we find there are 24 terms of the form (3.8). This corresponds to the number of permutations of four distinguishable elements. The Hamiltonian for this interaction is then written as

$$H = \frac{24}{2^5}\varepsilon_0\chi^{(3)}\int_V E_{1+}^{(+)} E_{2-}^{(+)} E_{s-}^{(-)} E_{i+}^{(-)}\, dV = \frac{3}{4}\varepsilon_0\chi^{(3)}\int_V E_{1+}^{(+)} E_{2-}^{(+)} E_{s-}^{(-)} E_{i+}^{(-)}\, dV \tag{3.9}$$

We assume that pump 1 and idler photons propagate in the positive z-direction, while pump 2 and signal photons propagate in the negative z-direction.

Since we are dealing with a spontaneous process, where there are no stimulating signal or idler fields and they arise from vacuum fluctuations, it is necessary to work within the framework of quantum optics. Then, we consider the pump fields as classical functions, while the signal and idler fields are treated as quantum operators. The Hamiltonian is therefore expressed as

$$\hat{H} = \frac{3}{4}\varepsilon_0 \chi^{(3)} \int_V E_{1+}^{(+)} E_{2-}^{(+)} \hat{E}_{s-}^{(-)} \hat{E}_{i+}^{(-)} \, dV \tag{3.10}$$

The pump laser fields in a waveguide can be expressed as [34]

$$\begin{aligned} E_{1+}^{(+)} &= E_1 f_1(x,y) \int \alpha_1(\omega) e^{i(\beta_1(\omega)z - \omega t)} d\omega \\ E_{2-}^{(+)} &= E_2 f_2(x,y) \int \alpha_2(\omega) e^{i(-\beta_2(\omega)z - \omega t)} d\omega \end{aligned} \tag{3.11}$$

where $\alpha(\omega)$ represents the spectral envelope of the laser pump, and $f(x,y)$ is the transverse field distribution of the guided mode, satisfying the normalization condition $\int f^2(x,y)dxdy = 1$. For the signal and idler fields, their corresponding operators are obtained from equation (2.14)

$$\begin{aligned} \hat{E}_{s-}^{(-)}(\boldsymbol{r},t) &= -i\sqrt{\delta k} f_s(x,y) \sum_{\beta_s} \exp\left[i(-\beta_s z + \omega t)\right] \ell(\omega) \hat{a}^\dagger(\beta_s) \\ \hat{E}_{i+}^{(-)}(\boldsymbol{r},t) &= -i\sqrt{\delta k} f_i(x,y) \sum_{\beta_i} \exp\left[i(\beta_i z + \omega t)\right] \ell(\omega) \hat{a}^\dagger(\beta_i) \end{aligned} \tag{3.12}$$

Substituting (3.11) and (3.12) into (3.10), we obtain

$$\begin{aligned} \hat{H}(t) = &-\frac{3}{4}\varepsilon_0 \chi^{(3)} E_1 E_2 \delta k \left[\int \int f_1 f_2 f_i f_s \, dxdy \right] \\ &\times \sum_{\beta_s} \sum_{\beta_i} \int \int d\omega_1 d\omega_2 \ell(\omega_s) \ell(\omega_i) \alpha_1(\omega_1) \alpha_2(\omega_2) \\ &\times e^{-i[\omega_1 + \omega_2 - \omega_i - \omega_s]t} \int_0^L dz e^{i(\beta_1 - \beta_2 + \beta_i - \beta_s)z} \hat{a}_s^\dagger \hat{a}_i^\dagger \end{aligned} \tag{3.13}$$

The overlap integral [34], phase mismatch, and frequency mismatch are given by the following expressions:

$$f_{eff} = \int\int f_1 f_2 f_i f_s \, dxdy \tag{3.14}$$

$$\Delta\beta = \beta_1 - \beta_2 + \beta_i - \beta_s \tag{3.15}$$

$$\Delta\omega = \omega_1 + \omega_2 - \omega_i - \omega_s \tag{3.16}$$

The z-integral has a simple closed form:

$$\int_0^L dz e^{i\Delta\beta z} = L e^{i\frac{\Delta\beta L}{2}} \operatorname{sinc}\left(\frac{\Delta\beta L}{2}\right) \tag{3.17}$$

Using (3.14)-(3.17) in (3.13), the Hamiltonian for the CP-SFWM process becomes

$$\begin{aligned} \hat{H}(t) = -\frac{3}{4}\varepsilon_0 \chi^{(3)} E_1 E_2 L \delta k f_{eff} \sum_{\beta_s}\sum_{\beta_i} \ell(\omega_s)\ell(\omega_i) \\ \times \int\int d\omega_1 d\omega_2 \alpha_1(\omega_1)\alpha_2(\omega_2) e^{-i\Delta\omega t} e^{i\frac{\Delta\beta L}{2}} \operatorname{sinc}\left(\frac{\Delta\beta L}{2}\right) \hat{a}_s^\dagger \hat{a}_i^\dagger \end{aligned} \tag{3.18}$$

This is the general Hamiltonian of the CP-SFWM process.

3.2 Hamiltonian of the CP-SFWM Process in a Ring Resonator

When considering the CP-SFWM process occurring in a ring cavity, the treatment is analogous to that presented in Section 3.1, considering the interaction length in this configuration corresponds to the cavity circumference, $L = 2\pi R$. However, it is necessary to formulate the problem in

cylindrical coordinates (r,h,θ). In this case, the transverse field distributions and the overlap integral are expressed in terms of (r,h) as follows

$$f_{eff} = \int\int f_1(r,h) f_2(r,h) f_s(r,h) f_i(r,h) dr dh \tag{3.19}$$

Assuming the radius of the ring resonator is not too small, on the order of hundreds of micrometers or larger, the guided mode in the ring can be considered approximately identical to that in a straight waveguide. Thus, we can make the following approximation:

$$\int\int f_1(r,h) f_2(r,h) f_s(r,h) f_i(r,h) dr dh \approx \int\int f_1(x,y) f_2(x,y) f_s(x,y) f_i(x,y) dx dy \tag{3.20}$$

To use the photon pairs in an experiment, they need to be extracted from the ring cavity. This is achieved via evanescent field coupling between the guided modes of the ring and a straight waveguide placed in close proximity to the cavity. Figure 3.1 illustrates a 2D schematic of this process.

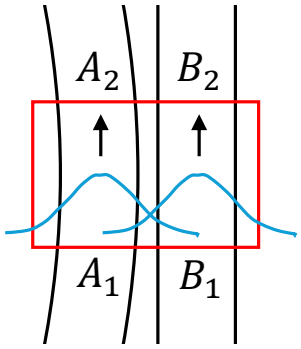

Fig. 3.1 A system comprising a ring cavity placed near a straight waveguide. The ring waveguide is shown on the left, while the straight waveguide is on the right. Blue lines represent the transverse field distributions of the guided modes, which extend beyond the waveguides, enabling interaction. Pairs (A_1, B_1) and (A_2, B_2) denote field amplitudes before and after the interaction region, respectively. Fields propagate from bottom to top.

In this configuration, the interaction region [108], red rectangle, allows guided modes propagating along one waveguide to excite modes in the other. Thus, photons can transfer

between the waveguides. The field amplitudes in this region are related through the scattering matrix [109]

$$\begin{bmatrix} A_2 \\ B_2 \end{bmatrix} = \begin{bmatrix} r & t \\ t & r \end{bmatrix} \begin{bmatrix} A_1 \\ B_1 \end{bmatrix} \tag{3.21}$$

Here, t and r are the transmission and reflection coefficients, respectively. In a general treatment these coefficients are complex, but we assume no phase shift occurs in the interaction, then we treat them as real values. Additionally, assuming energy conservation in the interactions, the coefficients satisfy $t^2 + r^2 = 1$. The squares of these coefficients can be interpreted as the probabilities of a photon remaining in the same waveguide (reflectivity) or transferring to the other (transmissivity).

To establish the relationship between the total field at the output of the bus waveguide and the field inside the cavity, we consider an infinitesimal region Δ of the bus waveguide, see Figure 3.2.

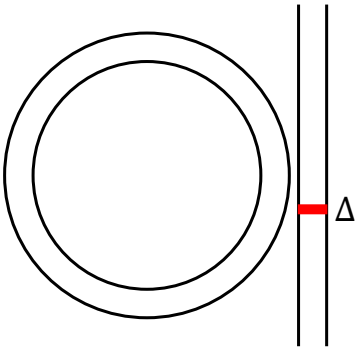

Fig. 3.2 Infinitesimal region, depicted in red, for the analysis of the field

At a given moment, the field amplitude in this region corresponds to the field just transferred from the ring to the bus waveguide, tE, as given by (3.21). If the system has reached a steady state, the field also includes contributions from previous rounds in the ring, with the respective phase accumulated during each round trip.

$$B = tA + trAe^{i\beta L} + tr^2Ae^{i2\beta L} + tr^3Ae^{i3\beta L} + \cdots \tag{3.22}$$

Here, the coefficients of r account for the field remaining in the ring after each interaction. This expression can be rewritten as

$$B = tA\sum_{n=0}^{\infty}\left(re^{i\beta L}\right)^n \tag{3.23}$$

Since $r < 1$, this is a geometric series that converges to

$$B = \frac{t}{1 - re^{i\beta L}}A \tag{3.24}$$

This function is known as the Airy function [87] of the cavity-bus waveguide system

$$\mathscr{A}(\beta) = \frac{t}{1 - re^{i\beta L}} \tag{3.25}$$

and it plays a significant role in determining the spectral properties and emission rate of the photon-pair source.

We explained the relation of classical fields in the system ring-bus waveguide, but the same applies for Fock states. Let $\hat{b}^\dagger$ represent the photon creation operator for the fundamental mode of the bus straight waveguide. It relates to the creation operator of the ring cavity, $\hat{a}^\dagger$, by

$$\hat{a}^\dagger(\beta) \to \mathscr{A}(\beta)\hat{b}^\dagger(\beta) \tag{3.26}$$

Thus, using (3.26) in (3.18) for signal and idler photons, the Hamiltonian of the entire system is given by

$$\begin{aligned}\hat{H}(t) = &-\frac{3}{4}\varepsilon_0\chi^{(3)}E_1E_2L\delta k f_{eff}\sum_{\beta_s}\sum_{\beta_i}\ell(\omega_s)\ell(\omega_i)\mathscr{A}_s(\omega_s)\mathscr{A}_i(\omega_i)\\ &\times\int\int d\omega_1 d\omega_2\alpha_1(\omega_1)\alpha_2(\omega_2)e^{-i\Delta\omega t}e^{i\frac{\Delta\beta L}{2}}\,\mathrm{sinc}\left(\frac{\Delta\beta L}{2}\right)\hat{b}_s^\dagger\hat{b}_i^\dagger\end{aligned} \tag{3.27}$$

3.3 Quantum State of Photons Generated by CP-SFWM in a Resonant Ring Cavity

To obtain the quantum state produced by the CP-SFWM process, we use a first order approximation derived from a perturbation scheme, where the state after a time t is given by [110]

$$|\psi\rangle = \left[1 - \frac{i}{\hbar}\int_0^t \hat{H}(t')dt'\right]|0\rangle\,|0\rangle \tag{3.28}$$

where $|0\rangle\,|0\rangle$ represents the vacuum for signal and idler modes corresponding to state at time $t = 0$. Notice in equation (3.27) the frequency mismatch (3.16) corresponds to energy conservation since CP-SFWM is a parametric process. If we consider the time τ, in which signal and idler photons are created via SFWM, is small compared to the integration window, $\tau << t$, we can consider the time integral defines a Dirac delta,

$$\int_0^t e^{-\Delta\omega t}dt = 2\pi\delta(\Delta\omega), \tag{3.29}$$

and using the property $\int f(x)\delta(x-a)dx = f(a)$ of the Dirac delta, we obtain the state of photon pairs generated by CP-SFWM

$$\begin{aligned} |\psi'\rangle &= \xi\,\delta k \sum_{\beta_s}\sum_{\beta_i} \ell(\omega_s)\ell(\omega_i)\mathscr{A}_s(\omega_s)\mathscr{A}_i(\omega_i) \\ &\times \int d\omega_2\,\alpha_1(\omega_s+\omega_i-\omega_2)\alpha_2(\omega_2)e^{i\frac{\Delta\beta L}{2}}\,\mathrm{sinc}\left(\frac{\Delta\beta L}{2}\right)\hat{b}_s^\dagger\hat{b}_i^\dagger\,|0\rangle\,|0\rangle \end{aligned} \tag{3.30}$$

where we defined the factor

$$\xi = \frac{6}{4}\pi\varepsilon_0\chi^{(3)}E_1E_2Lf_{eff} \tag{3.31}$$

This is the general form of the state of photon pairs generated by CP-SFWM in a resonant ring cavity.

3.4 Spectral Properties

As mentioned earlier, we are working within the mixed scheme of CP-SFWM, this is, pump 2 is considered a continuous-wave laser with narrow bandwidth. Thus, its spectral envelope can be approximated as a Dirac delta. Equation (3.30) is rewritten as:

$$\begin{aligned} |\psi'\rangle = \xi\,\delta k \sum_{\beta_s}\sum_{\beta_i} \ell(\omega_s)\ell(\omega_i)\mathscr{A}_s(\omega_s)\mathscr{A}_i(\omega_i) \\ \times \alpha_1(\omega_s+\omega_i-\omega_2^0) e^{i\frac{\Delta\beta L}{2}} \operatorname{sinc}\left(\frac{\Delta\beta L}{2}\right) \hat{b}_s^\dagger \hat{b}_i^\dagger |0\rangle\,|0\rangle \end{aligned} \tag{3.32}$$

where ω_2^0 denotes the central frequency of pump 2. In this expression, we differ in the argument of the exponential function from the one obtained in [66], where they analyze the CP-SFWM process in an optical fiber. We find that the exponential term depends on the phase mismatch Δk, with the same argument as the $sinc()$ function, which is commonly reported in studies on SPDC and SFWM photon sources [34, 36, 87, 111]. In contrast, their equation defines the exponential in terms of a different parameter, κ, which corresponds to the sum of the propagation constants rather than the phase mismatch. This difference does not ultimately affect the spectral characterization of photon pairs, as it merely introduces a phase factor that does not appear in the squared norm of the summand in Equation (3.32), which dictates the spectral properties of the photons. Since the functions $\ell(\omega)$ vary slowly, their influence is considered negligible. Therefore, the spectral properties are determined by

$$|G(\omega_s,\omega_i)|^2 = \left|\mathscr{A}_s(\omega_s)\mathscr{A}_i(\omega_i)\alpha_1(\omega_s+\omega_i-\omega_2^0)\operatorname{sinc}\left(\frac{\Delta\beta L}{2}\right)\right|^2. \tag{3.33}$$

This is the so-called Joint Spectral Intensity (JSI) function of the process. This function plays a crucial role for the characterization of the photon source as it provides information of the spectral entanglement of the photon pairs, and it serves as a basis for estimating the photon emission rate.

3.4.1 The Schmidt Decomposition

The Schmidt decomposition is a mathematical tool useful for analyzing bipartite quantum systems. It provides a way to quantify the degree of entanglement between the two subsystems [112, 113]. In a quantum system composed of two subsystems, denoted by $\boldsymbol{A}$ and $\boldsymbol{B}$, with respective Hilbert spaces $\mathscr{H}_A$ and $\mathscr{H}_B$, the total Hilbert space of the composite system is $\mathscr{H} = \mathscr{H}_A \otimes \mathscr{H}_B$. A pure state of the composite system $|\psi\rangle \in \mathscr{H}$, is expressed as

$$|\psi\rangle = \sum_{i,j} c_{i,j} |a_i\rangle \otimes |b_j\rangle \tag{3.34}$$

The Schmidt theorem states that the state can be re-expressed as a sum of the form

$$|\psi\rangle = \sum_{i} \sqrt{\lambda_i} |u_i\rangle \otimes |v_i\rangle \,, \tag{3.35}$$

where the coefficients satisfy $\sum_i \lambda_i = 1$, and $|u_i\rangle$ and $|v_i\rangle$ are orthonormal bases of the subsystems $\boldsymbol{A}$ and $\boldsymbol{B}$, respectively. This is known as the Schmidt decomposition [112].

To quantify the degree of entanglement, two parameters are commonly used: K, the effective Schmidt number, and P, the purity. These parameters are related by $P = 1/K$. In this work, we use the purity P, defined as [114]

$$P = \sum_i \lambda_i^2 \tag{3.36}$$

since it is a normalized parameter and provides an intuitive measure of how "pure" each subsystem is, depending on its value $P \in [0,1]$. The physical interpretation of this parameter is as follows:

- $P = 1$, the decomposition contains only one term, $\lambda_1 = 1$ and all other $\lambda_i = 0$, corresponding to a separable non-entangled state.
- $P < 1$, the decomposition includes more than one term, indicating entanglement.

Then, for a pure global state $|\psi\rangle \in \mathscr{H}$, entanglement implies a loss of purity in the subsystems. For photon pair sources based on parametric processes, the generated photon-pair states are often entangled in frequency. To quantify the degree of frequency correlation, the Schmidt decomposition is applied to the Joint Spectral Intensity [114]. In the case of non-entangled photon pairs, the JSI satisfies

$$|G(\omega_s,\omega_i)|^2 = |G_s(\omega_s)|^2|G_i(\omega_i)|^2 \tag{3.37}$$

3.5 Photon Pair Emission Rate

The emission rate of the photon source is determined by the expectation of the photon number for all the modes, given by [87]

$$N_p = R\sum_{\beta_{s''}} \langle\psi'|\,\hat{a}^\dagger_{s''}\hat{a}_{s''}\,|\psi'\rangle \tag{3.38}$$

As shown in (3.31), the state is expressed in terms of the pump field amplitude for a single pulse. Therefore, in equation (3.38), we multiply the summation by R, the pulse rate per second of the pulsed laser. We rewrite equation (3.38) substituting (3.32).

$$\begin{aligned} N_p =& R|\xi|^2(\delta k)^2 \sum_{\beta_{s'}}\sum_{\beta_{i'}}\sum_{\beta_{s''}}\sum_{\beta_s}\sum_{\beta_i} \langle 0|\,\langle 0|\,\hat{a}_{s'}\hat{a}_{i'}\hat{a}^\dagger_{s''}\hat{a}_{s''}\hat{a}^\dagger_s\hat{a}^\dagger_i\,|0\rangle\,|0\rangle \\ &\times \ell(\omega_{s'})\ell(\omega_{i'})G(\omega_{s'},\omega_{i'})\ell(\omega_s)\ell(\omega_i)G^*(\omega_s,\omega_i) \end{aligned} \tag{3.39}$$

In equation (3.39), $G(\omega_s,\omega_i)$ represents the Joint Spectral Amplitude (JSA), and the notation $G^*()$ denotes its complex conjugate. We simplify equation (3.39) using the algebra of creation and annihilation operators.

$$\begin{aligned} N_p =& R|\xi|^2(\delta k)^2 \sum_{\beta_{i'}}\sum_{\beta_i}\sum_{\beta_{s'}}\sum_{\beta_{s''}}\sum_{\beta_s} \langle 0|\,\hat{a}_{i'}\hat{a}_i^\dagger\,|0\rangle\,\langle 0|\,\hat{a}_{s'}\hat{a}_{s''}^\dagger\hat{a}_{s''}\hat{a}_s^\dagger\,|0\rangle \\ &\times \ell(\omega_{s'})\ell(\omega_{i'})G(\omega_{s'},\omega_{i'})\ell(\omega_s)\ell(\omega_i)G^*(\omega_s,\omega_i) \end{aligned} \tag{3.40}$$

We perform the operations on the vacuum state, with which the expression can be rewritten as

$$\begin{aligned} N_p =& R|\xi|^2(\delta k)^2 \sum_{\beta_{i'}}\sum_{\beta_i}\sum_{\beta_{s'}}\sum_{\beta_{s''}}\sum_{\beta_s} \langle 1|_{i'}\,|1\rangle_i\,\langle 1|_{s'}\,\hat{a}_{s''}^\dagger\hat{a}_{s''}\,|1\rangle_s \\ &\times \ell(\omega_{s'})\ell(\omega_{i'})G(\omega_{s'},\omega_{i'})\ell(\omega_s)\ell(\omega_i)G^*(\omega_s,\omega_i) \end{aligned} \tag{3.41}$$

In equation (3.41), the term $\langle 1|_{i'}\,|1\rangle_i$ corresponds to a Kronecker delta $\delta_{i,i'}$, the remaining operators correspond to the number operator $\hat{n}_{s''}$ for which we have the relation $\hat{n}_{s''}\,|1\rangle_s = \delta_{s,s''}\,|1\rangle_s$. We can drop summations on i' and s'', then, equation (3.41) rewrites as

$$N_p = R|\xi|^2(\delta k)^2 \sum_{\beta_i}\sum_{\beta_{s'}}\sum_{\beta_s} \langle 1|_{s'}\,|1\rangle_s\,\ell(\omega_{s'})\ell(\omega_i)G(\omega_{s'},\omega_i)\ell(\omega_s)\ell(\omega_i)G^*(\omega_s,\omega_i) \tag{3.42}$$

The operation $\langle 1|_{s'}\,|1\rangle_s$ corresponds to another Kronecker delta, $\delta_{s,s'}$, with which we drop the summation on s'.

$$N_p = R|\xi|^2(\delta k)^2 \sum_{\beta_i}\sum_{\beta_s} \ell(\omega_s)\ell(\omega_i)G(\omega_s,\omega_i)\ell(\omega_s)\ell(\omega_i)G^*(\omega_s,\omega_i) \tag{3.43}$$

The expression of the emission rate is written in terms of the JSI as:

$$N_p = R|\xi|^2(\delta k)^2 \sum_{\beta_s}\sum_{\beta_i} \ell^2(\omega_s)\ell^2(\omega_i)|G(\omega_s,\omega_i)|^2 \tag{3.44}$$

Lastly, we substitute in (3.44) the formulae for third-order nonlinearity in terms of the nonlinear refractive index [107], the nonlinear coefficient definition [115], and the power of continuous-wave and pulsed lasers in terms of their field amplitudes [116]

$$\chi^{(3)} = \frac{4}{3} c\varepsilon_0 n_{eff}(\omega_1) n_{eff}(\omega_2) n^{(2)} \tag{3.45}$$

$$\gamma = \frac{n^{(2)} f_{eff} \sqrt{\omega_1 \omega_2}}{c} \tag{3.46}$$

$$P_2 = \frac{1}{2} n_{eff}(\omega_2) \varepsilon_0 c |E_2|^2 \tag{3.47}$$

$$P_1 = \frac{n_{eff}(\omega_1) \varepsilon_0 c |E_1|^2}{2R\delta} \tag{3.48}$$

where $n^{(2)}$ denotes the nonlinear refractive index of Si_3N_4, δ and R are the pulse time-width and repetition rate of pump 1, respectively, and $n_{eff}(\omega_1)$ and $n_{eff}(\omega_2)$ are the effective refractive index of the guided modes for pumps 1 and 2, respectively. With this, we obtain an expression for the emission rate in terms of material and experimental parameters:

$$N_p = \frac{2^5 c^2 n_1 n_2 L^2 \gamma^2 P_1 P_2}{\omega_1 \omega_2 \delta} (\delta k)^2 \sum_{\beta_s} \sum_{\beta_i} \frac{\omega_s \omega_i}{n_{eff}^2(\omega_s) n_{eff}^2(\omega_i)} |G(\omega_s, \omega_i)|^2 \tag{3.49}$$

Finally, by considering the quantization length $L_Q \to \infty$, the summations are converted into integrals using $\delta k \sum \to \int dk$ [34], and since the calculations are performed in terms of angular frequencies, we substitute $\int dk \to \int \beta^{(1)}(\omega) d\omega$, where the superscript denotes the first derivative. Thus, the emission rate is expressed as:

$$N_p = \frac{2^5 c^2 n_1 n_2 L^2 \gamma^2 P_1 P_2}{\omega_1 \omega_2 \delta} \int \int \frac{\omega_s \omega_i \beta^{(1)}(\omega_s) \beta^{(1)}(\omega_i)}{n_{eff}^2(\omega_s) n_{eff}^2(\omega_i)} |G(\omega_s, \omega_i)|^2 d\omega_s d\omega_i \tag{3.50}$$

Chapter 4

Optimization of the Source's Parameters and Characterization

In this chapter, we present a detailed description of the complete design process of our photon source, along with the simulation results for the emission rate and spectral properties. We set the wavelengths for our photon source as follows: 800 nm for pump 1-signal and 1550 nm for pump 2-idler. These specific wavelengths were chosen because our facilities are equipped with lasers that operate at these values. The process of defining the geometric parameters consists of three key steps:

1. Identify the ideal transverse dimensions of the waveguides to maximize the photon-pair generation rate.

2. Select a ring-resonator radius that satisfies the resonance conditions for the signal and idler wavelengths.

3. Determine the optimal coupling gaps between the bus waveguides and the ring to achieve the desired quality factor.

4.1 Sample Features and Waveguide Width Optimization

The proposed photon source comprises a silicon nitride-on-insulator microring resonator in an add-drop configuration (see Figure 2.3). The sample considered for the design consists of a silicon (Si) wafer, with a layer of silicon dioxide (SiO_2), and a top layer of silicon nitride (Si_3N_4) with a height of $h = 430$ nm, see Figure 4.1. This specific material and height can be etched using our reactive ion etching equipment.

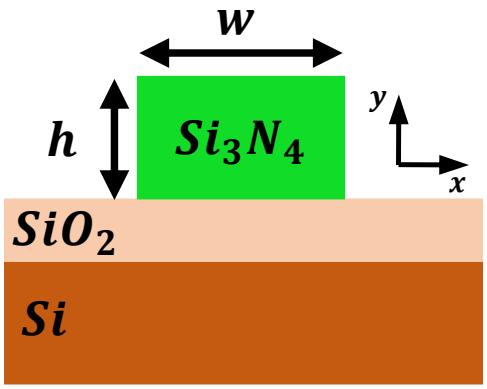

Fig. 4.1 Schematic of the cross section of the sample.

Then, since the height of the waveguides is set to a fixed parameter, we need to determine the width (w) of the waveguide and the radius (R) of the ring resonator. Although the phase matching condition in the CP-SFWM scheme is satisfied for any waveguide geometry that supports guided modes at the signal (pump 1) and idler (pump 2) wavelengths, we will select the waveguide width that maximizes the photon-pair emission rate, as explained below. To achieve this, we used the WGMODES solver [117] to calculate for several waveguide widths the eigenmodes, their transverse field distributions and wave vectors,

$$\beta(\lambda) = n_{\text{eff}}(\lambda)\frac{2\pi}{\lambda}, \tag{4.1}$$

at the signal (pump 1) and idler (pump 2) frequencies. In equation (4.1), $n_{eff}(\lambda)$ is the effective refractive index of the guided mode.

In Figure 4.2, we present the effective refractive indices for waveguide widths ranging from 634 nm to 1100 nm. Additionally, the bulk refractive indices of Si_3N_4 (navy-blue line) and SiO_2 (red line) are also shown, calculated using their respective Sellmeier equations [118, 119].

$$n_{Si_3N_4}(\lambda) = \sqrt{1 + \frac{3.0249\lambda^2}{\lambda^2 - 0.1353406^2} + \frac{40314\lambda^2}{\lambda^2 - 1239.842^2}} \tag{4.2}$$

$$n_{SiO_2}(\lambda) = \sqrt{1 + \frac{0.6961663\lambda^2}{\lambda^2 - 0.0684043^2} + \frac{0.4079426\lambda^2}{\lambda^2 - 0.1162414^2} + \frac{0.8974794\lambda^2}{\lambda^2 - 9.896161^2}} \tag{4.3}$$

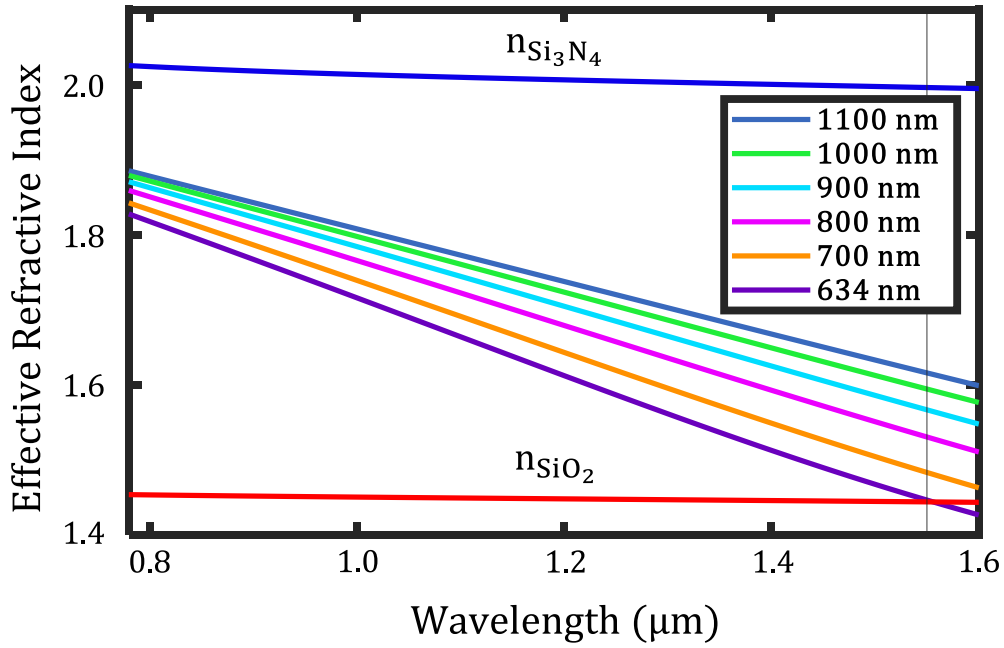

Fig. 4.2 Effective refractive index of the TE_{00} mode as a function of wavelength for different waveguide widths ($h = 430\ nm$). The vertical line is set at $\lambda = 1.55\ \mu m$. The refractive indices of SiO_2 (navy-blue line) and Si_3N_4 (red line) are also plotted.

It is well known that a guided mode is supported when the effective refractive index lies between the refractive indices of the core and cladding materials [120], that is, when the condition $n_{Si_3N_4} > n_{eff} > n_{SiO_2}$ is satisfied. Our simulations indicate that for waveguides with widths smaller than 634 nm, the condition $n_{eff} > n_{SiO_2}$ is not satisfied. As shown in Figure 4.2, the purple line ($w = 634\ nm$) lies slightly above the red line (cladding refractive index) at 1550

nm. Consequently, waveguides with widths below 634 nm cannot support a guided mode at $\lambda = 1550$ nm, establishing this value as a lower boundary. The full set of simulations included waveguides with widths ranging from less than 634 *nm* to more than 1100 *nm*, using a step size of 1 *nm*. However, the graph does not display all simulations, as the selected data points are sufficient to reveal the relevant trends while preventing the graph from being saturated.

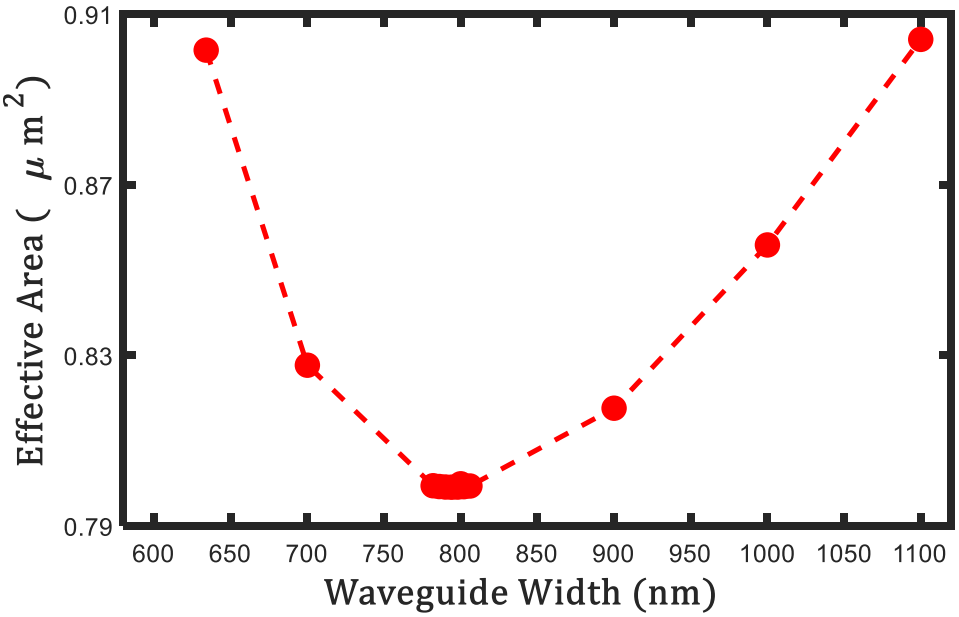

Fig. 4.3 Effective interaction area A_{eff} as a function of the waveguide width. The lines are used to join the calculated points for discrete values of the waveguide width. The minimal value of A_{eff} was obtained for a waveguide width of $w = 794$ *nm*.

Afterwards, we simulated the transverse electric field distributions for the TE_{00} mode at the signal and idler wavelengths for various waveguide widths, ranging from 634 nm to 1100 nm. These field distributions were used to compute the overlap integral, given by equation (3.14). At this point it is convenient to mention that the overlap integral is inversely related to the effective area of the SFWM interaction, $A_{eff} = f_{eff}^{-1}$. Therefore, the objective was to determine the waveguide width that minimizes the effective area, as the photon emission rate is related to this parameter as $N_p \sim 1/A_{eff}^2$ (see equations (3.50) and (3.46)). This relationship arises because a smaller overlap area between the transverse field distributions of the modes, indicating

more confined energy, leads to a greater interaction of pump photons, thereby increasing the pair production rate. In Figure 4.3, we show the calculated values of A_{eff}. We observe that the effective area decreases as the waveguide width is reduced until it reaches a minimum at $w = 794\ nm$. Beyond this point, however, the trend reverses, and the effective area begins to increase again. To explain this behavior, in Figure 4.4 a), b), and c) we show the transverse field distribution for three different waveguide widths: 1100 nm, 794 nm, and 634 nm, respectively for $\lambda = 800\ nm$ in the left column and $\lambda = 1550\ nm$ in the right column.

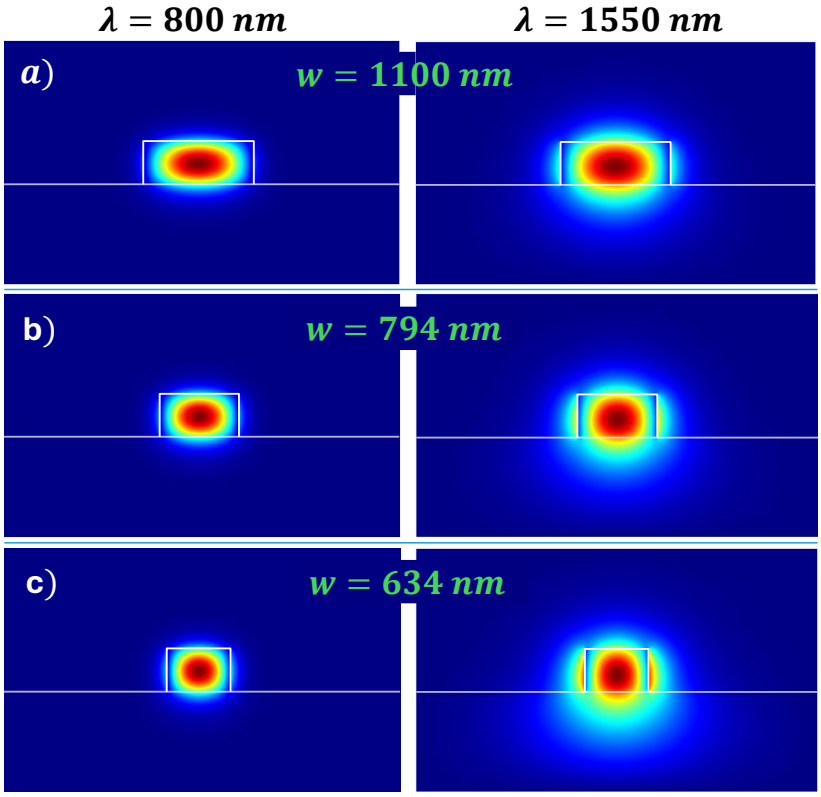

Fig. 4.4 Transverse electric field distributions for the TE_{00} modes at $\lambda = 800\ nm$ and $\lambda = 1550\ nm$ (left, right columns) for waveguides with width (a) 1100 nm, (b) 794 nm, (c) 634 nm, with a fixed height of 430 nm. We highlighted the field distribution for a waveguide of width w = 794 nm, which we identified as a preliminary optimal width for our device.

For the mode at $\lambda = 800\ nm$, the area of its field distribution exhibits a monotonic decrease as the waveguide width decreases in the range of simulated values. For the mode at $\lambda = 1550\ nm$, we observe that its area at $w = 794\ nm$ is smaller than the one at $w = 1100\ nm$, similar to

the behavior observed for the mode at $\lambda = 800\,nm$. However, for $w = 634\ nm$, the field distribution area does not follow this tendency; it is larger than the area at $w = 794\ nm$, even though the waveguide's cross-sectional size is smaller. In Figure 4.2, we observed that as the waveguide width approaches 634 *nm*, the condition to support a guided mode is compromised for $\lambda = 1550\ nm$. Simulations of the transverse field distributions reveal that this occurs because the guided mode becomes less confined near this width.

Based on this analysis, we set $w = 794\ nm$ as a preliminary optimal waveguide width, as this value yields the minimum effective area. We conclude that the optimal waveguide width is not necessarily the smallest width for which guided modes are supported; instead, it requires a systematic exploration to identify the optimal value.

4.2 Optimization of Microring Radius and Photon Emission Rate

The next step is to determine a suitable radius for each waveguide width simulated in the previous section and computing the photon emission rate using equation (3.50). The optimal pair radius-waveguide width corresponds to the one for which the emission rate is maximized. For a waveguide of a given width, a suitable radius, R, is defined as one for which both the signal and idler photons are resonant within the cavity. Mathematically, this implies that the following condition must be satisfied for both wavelengths:

$$n_{eff}(\lambda)\frac{2\pi R}{\lambda} = l \tag{4.4}$$

where $l \in \mathbb{Z}$ represents the azimuthal mode number of the cavity. For each radius under consideration, this resonance condition was validated by identifying the closest resonant frequencies ($\bar{\omega}_s$, $\bar{\omega}_i$) and ensuring that the absolute differences for both the signal and idler frequencies satisfied the threshold condition:

$$|\bar{\omega}_{s,i} - \omega_{s,i}| < 2\pi(100\ MHz) \tag{4.5}$$

where $\bar{\omega}$ is the frequency of a resonance of the cavity.

The process is not straightforward due to the nonlinear variation of the effective refractive index of the guided modes (see Figure 4.2). Optimizing the radius to satisfy resonance for one wavelength does not guarantee resonance for the other. Therefore, a search range for the radii was defined between 140 μm and 160 μm, and the optimization process involved systematically varying the ring radii within this range in steps of $\Delta R = 0.0001\ \mu m$. At each step, condition (4.5) was evaluated for both wavelengths, and the radius for which both conditions were minimized was selected as optimal. The narrow search range was chosen to ensure consistent conditions when comparing photon-pair emission rates. Consistency is crucial because N_p depends on the radius of the cavity (see equation (3.50)). Specifically, a larger radius directly leads to a longer cavity length, L, which ultimately results in a higher emission rate. Therefore, significant variations in radius across different waveguide widths would lead to biased comparisons.

In order to compute photon emission rates, it is necessary to evaluate the Airy functions of resonances, equation (3.25), at signal and idler wavelengths to evaluate the integral (3.50). We considered a quality factor of $Q = 1.4 \times 10^6$, which is the highest value reported in literature for a silicon nitride microring resonator [121], and computed the respective reflection and transmission coefficients for the Airy functions using the relation [103]

$$r = 1 - \frac{\pi l}{Q} \tag{4.6}$$

where l is the azimuthal mode number for the respective resonances found for each waveguide.

Using the optimized radius obtained for each waveguide width and the Airy functions, we then calculated the photon-pair emission rate using equation (3.50), see Figure 4.5. The calculations were performed assuming pump lasers with Gaussian spectral envelope, $\alpha(\omega)$, centered at the signal and idler wavelength, respectively. Pump powers were set at $P_1 = P_2 =$

1 mW, and the spectral properties of two lasers available in our facilities: the Chameleon Vision II ($\delta = 140\ fs$, repetition rate $R = 80\ MHz$, $\sigma_1 = 1.874\ THz$) [122], and the TLB-6730 laser ($\sigma_2 = 200\ kHz$) [123].

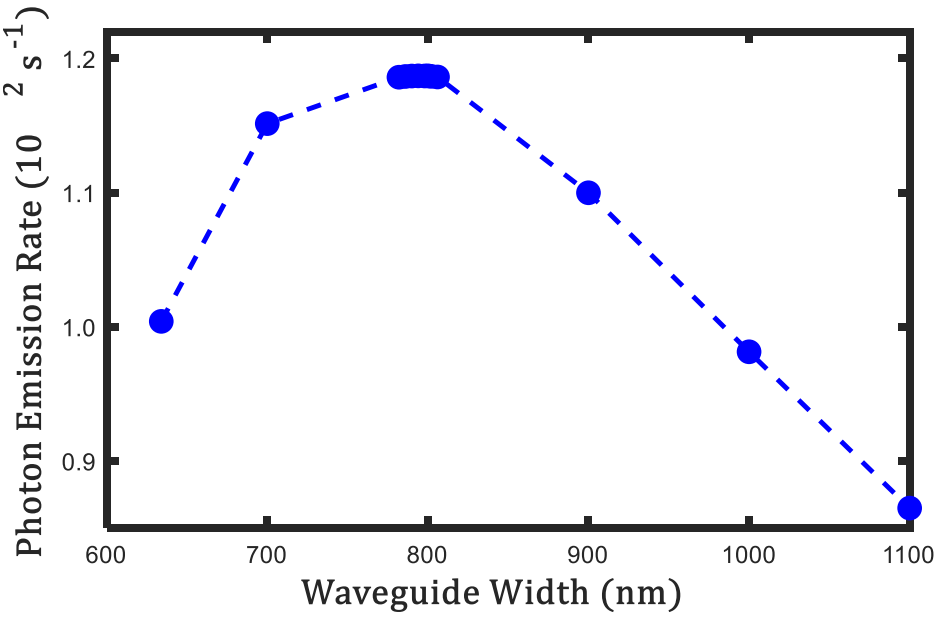

Fig. 4.5 Photon emission rate, N_p, as a function of the waveguide width. The maximal value corresponded for the waveguide of width of $w = 794\ nm$.

The photon emission rate has an expected tendency opposite to the effective area (see Figure 4.3), since they are related as $N_p \sim 1/A_{eff}^2$. However, we did not select $w = 794$ nm as the optimal value only based on the simulations of A_{eff}. As mentioned earlier, we predefined a reduced search space for the resonator radius to ensure consistency. Nevertheless, even within this constraint, the waveguide width that maximizes the photon emission rate may differ slightly from the one that minimizes the effective area. In Figures 4.3 and 4.5, the fine variations in waveguide width simulations around 800 nm can be observed. This refined search was conducted to capture potential small variations. The simulations revealed that the maximum photon-pair emission rate was $N_p = 118.70$ pairs/s, corresponding to a waveguide width of $w = 794$ nm and a ring resonator radius of $R = 156.34\ \mu m$.

4.3 Ring-Bus Waveguides Gaps Optimization

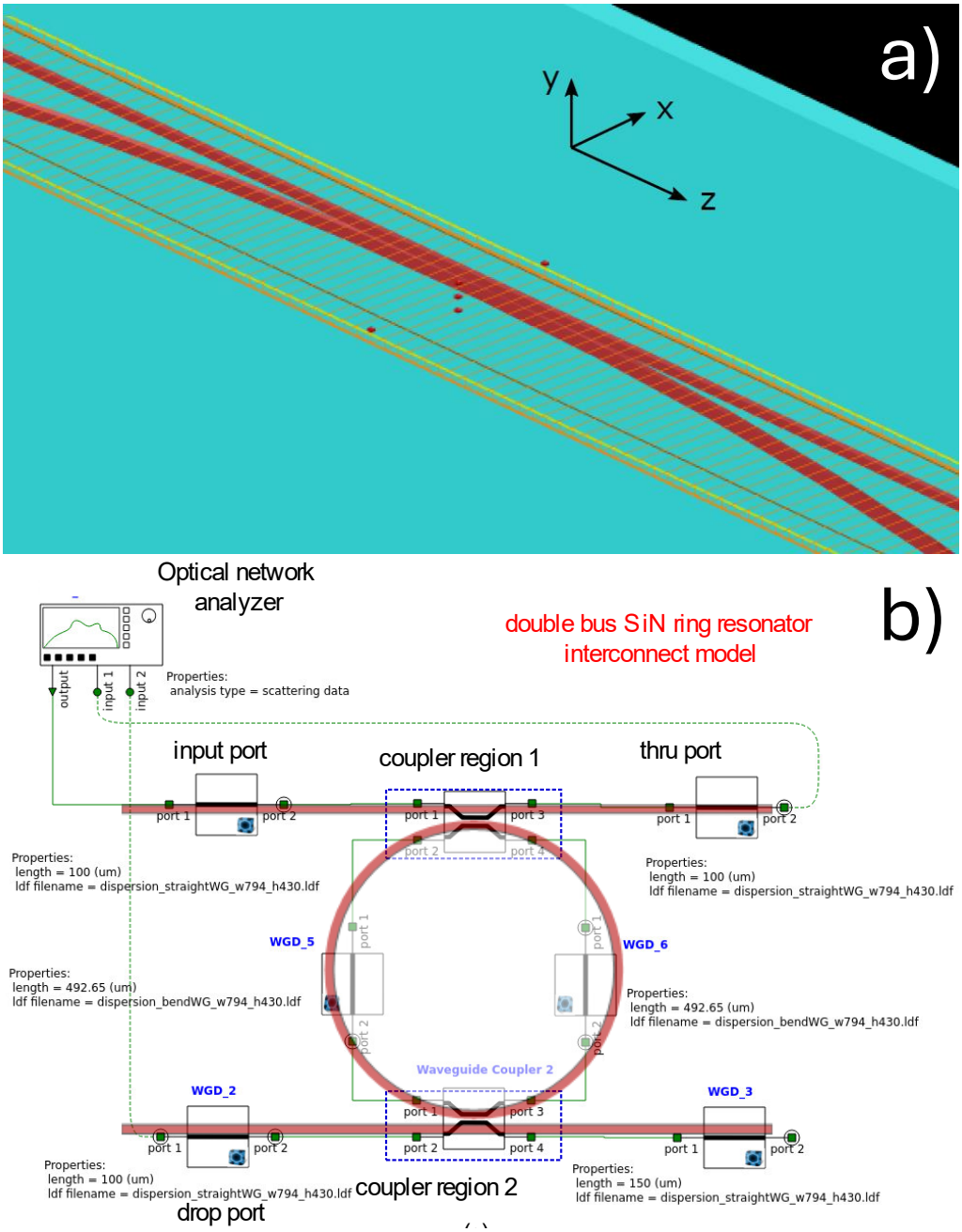

Fig. 4.6 a) Diagram in MODE illustrating a segment of the bus-ring waveguides that constitute a directional coupler. b) Schematic of the full microring resonator simulated in INTERCONNECT.

To finalize the design of the photon pair source, we used the MODE and INTERCONNECT modules from Ansys Lumerical software [124, 125] to determine the optimal gaps between the ring cavity and the bus waveguides. In these simulations, the ring resonator was modeled by decomposing it into multiple waveguide segments, including two directional couplers, straight waveguides, and bend waveguides. These individual components were then integrated into a circuit within the INTERCONNECT module to simulate the complete behavior of the resonator. Figure 4.6 illustrates the simulation setups in both MODE and INTERCONNECT.

The simulations began by identifying the guided modes using the eigenmode expansion (EME) solver. Next, the propagation characteristics of the straight and bend waveguides were analyzed using the finite difference method (FDM) in Mode Solution. Finally, the quality factors at the signal and idler wavelengths were characterized over a range of gap values through full simulations performed in INTERCONNECT. Figure 4.7 illustrates the simulation of pump field coupling from the bus waveguide to the ring cavity via the evanescent field, along with the transmission spectrum around 800 *nm* in which we can appreciate a resonance.

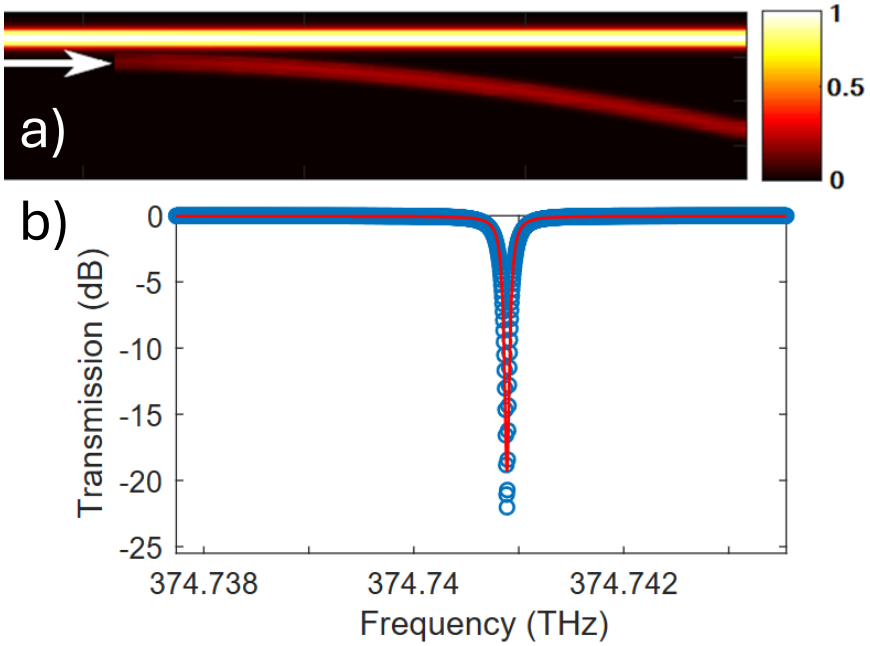

Fig. 4.7 a) Diagram showing the simulation of pump laser coupling from the bus waveguide to the microring. b) Transmission spectrum showing a resonance at 800 *nm*.

Then, we proceed to simulate the quality factor (Q) for resonances at signal and idler wavelengths, obtained with our proposed source by varying the gap between the bus waveguides and the microring cavity. For a given resonance, its corresponding quality factor is computed using the equation [109]:

$$Q = \frac{\nu}{\Delta\nu}, \tag{4.7}$$

where ν is the central frequency of the resonance, and $\Delta\nu$ is the full width at half maximum (FWHM). Figure 4.8 shows the characterization of the quality factors at signal and idler wavelengths across a gap range of 100 *nm* to 600 *nm*.

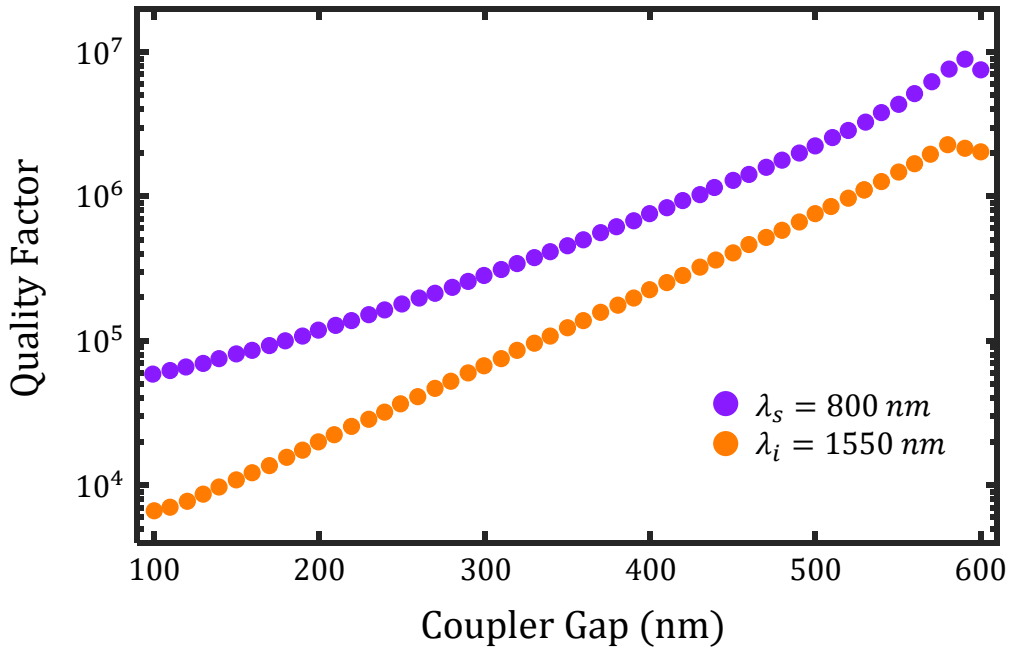

Fig. 4.8 Q-factor of the resonances at 800 nm and 1550 nm as a function of ring-bus waveguide gap.

The increasing tendency of the quality factor as the gap increases, followed by its subsequent decrease, can be explained using equations (3.21) and (4.6). The quality factor increases as r approaches one ($Q = \frac{\pi l}{1-r}$), meaning that radiation remains confined within the ring resonator

for a longer time, increasing the photon lifetime inside the cavity and enhancing amplification. However, if the ring and bus waveguide are too far apart, their evanescent fields no longer interact, which affects the coupling and causes the quality factor to decrease after a certain threshold [126]. The maximum achievable quality factors for the signal and idler were found to be $Q = 8.92 \times 10^6$ and $Q = 2.28 \times 10^6$, respectively. The corresponding gap values to achieve these maxima are 590 nm and 580 nm.

The Q-factor values obtained in the simulations exceed the highest reported value for a Si_3N_4 ring resonator, $Q = 1.4 \times 10^6$ [121]. For subsequent simulations of the photon emission rate and the spectral characteristics of the photons, we used the value $Q = 1.4 \times 10^6$ for both resonances. These ring-bus waveguide gaps complete the optimal geometric parameters for the proposed device.

4.4 Spectral Properties Characterization

In this section, we analyze the spectral properties of the photon pairs generated by the photon source, using the optimal parameters determined in the previous sections and considering the spectral characteristics of the lasers described in Section 4.2. Figure 4.9 a) shows the normalized JSI (Equation (3.33)) of the photon pairs produced by our photon source based on CP-SFWM. The color scale on the right represents the values of the JSI function, which correspond to the joint probability density of detecting photon pairs. The graph is centered at the frequencies $\nu_s = 374.74\ THz$ ($\lambda_s = 800\ nm$) and $\nu_i = 193.41\ THz$ ($\lambda_i = 1550\ nm$) within a 500 MHz square window. The optimization of the ring resonator's radius is evident in this graph. Photon pairs are effectively generated at the desired wavelengths, as we carefully selected the radius through an optimization process to ensure resonances located at these wavelengths. The precise tunability of the photon pair wavelengths is one of the key advantages of our scheme.

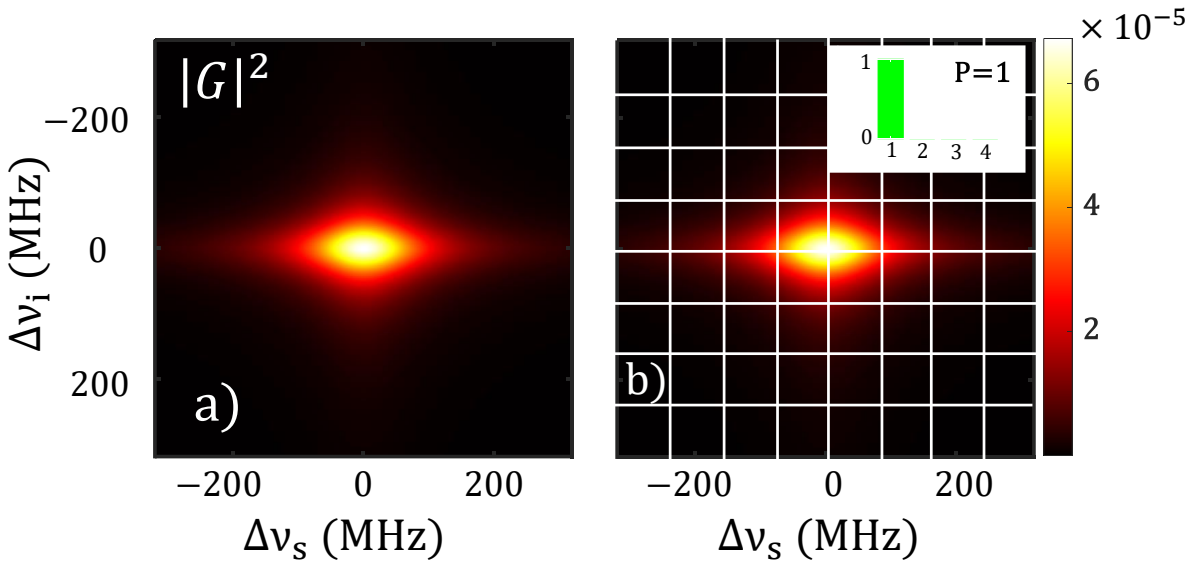

Fig. 4.9 a) JSI of CP-SFWM photon pairs generated in our proposed microring resonator source. b) Representation of a discrete JSI function using square sections.

To analyze the purity of the photon-pair state we computed a Schmidt decomposition of the JSI. Numerically, this was done by taking a discrete representation of the JSI, corresponding to a matrix, and applying a singular value decomposition (SVD) [114]. This numerical method involves representing a matrix A of dimensions $m \times n$ as a sum of $min(m,n)$ vector products, expressed as [127]:

$$A = \sum_{i}^{min(m,n)} \rho_i \boldsymbol{u}_i \boldsymbol{v}_i^T \tag{4.8}$$

where $\boldsymbol{u}_i$ are vectors of dimension m that span the column space, and $\boldsymbol{v}_i^T$ are vectors of dimension n that span the row space. The ρ_i are the singular values, which assign weights to each term in the matrix reconstruction. This description highlights the connection between SVD and the Schmidt decomposition. In Figure 4.9 b), we show a representation of the discretized JSI in square regions. The computation was carried out in MATLAB using a discretization of $m = 1200$ and $n = 1200$, corresponding to squares of $0.5\ MHz \times 0.5\ MHz$. The purity obtained

was $P = 1$, indicating a separable state. The inset in Figure 4.9 b) shows the first four Schmidt values; since the JSI is separable, the first element is 1, and the remaining 0.

Figures 4.10 a) and b) show the marginal distributions for the signal and idler photons, respectively, obtained by integrating the JSI over the other variable. That is, to obtain the marginal distribution of signal photons, we integrated the JSI over the idler variable, and vice versa. We obtained full-width at half-maximum (FWHM) bandwidths of $\Delta\nu_s = 157.9\ MHz$ and $\Delta\nu_i = 79.7\ MHz$ for the signal and idler photons. The idler photon bandwidth, $\Delta\nu_i = 79.7\ MHz$, achieved with a Q-factor of $Q = 1.4 \times 10^6$, is narrower than the bandwidth required for an efficient interaction with erbium-ion-based solid-state quantum memories ($\approx 185\ MHz$) [128]. This demonstrates that photon sources based on the CP-SFWM scheme in microring resonators are suitable for such applications, provided that a sufficiently high quality factor is achieved, as has been demonstrated with Si_3N_4 ring cavities [121].

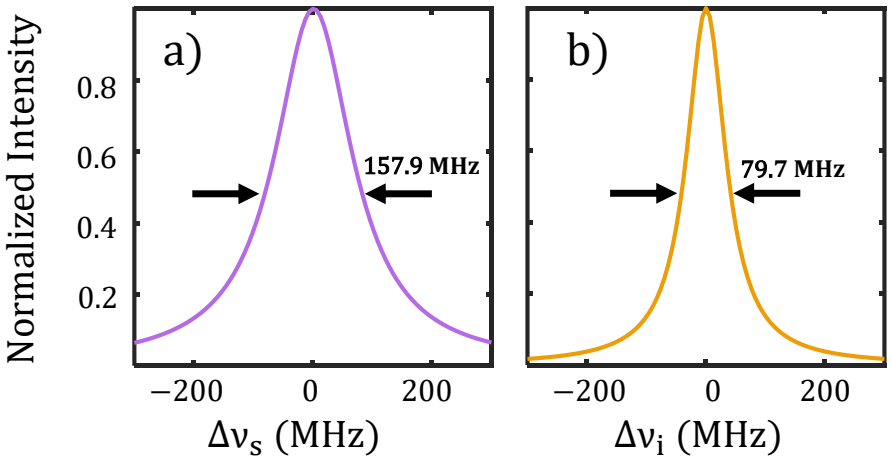

Fig. 4.10 Marginal distributions for a) signal photons (800 nm) with 157.9 MHz bandwidth and b) idler photons (1550 nm) with 79.7 MHz bandwidth.

For comparison, we replicated simulations of the CP-SFWM source based on optical fibers in the mixed case as reported in [66]. Using a Q-factor of $Q = 1.4 \times 10^6$ and pump powers $P_1 = P_2 = 1\ mW$, our source ($R = 156.34\ \mu m,\ L = 982.31\ \mu m$) is predicted to generate $N_p = 118.70\ pairs/s$ with a signal photon bandwidth of $\Delta\nu_s = 157.9\ MHz$ and an idler photon bandwidth of $\Delta\nu_i = 79.7\ MHz$. In comparison, adjusting the parameters from Monroy et

al. to match our pump powers, an optical fiber length of approximately 21.949 m would be required to achieve the same emission rate as our source, representing an enhancement factor of 2.23×10^4 in our design. Similarly, achieving the same signal photon bandwidth would require a fiber length of about 6.894 m, corresponding to an improvement factor of 7.02×10^3. These significant advancements in both emission rate and bandwidth reduction underscore the scalability and efficiency of our photon source design. In Table 4.1, we summarize the results of the comparison.

	Fiber length	Enhancement factor
$N_p = 118.70\ pairs/s$	21.949 m	2.23×10^4
$\Delta\nu_s = 157.9\ MHz$	6.894 m	7.02×10^3

Table 4.1 Fiber lengths needed to achieve the performance of our integrated photon source.

4.5 Analysis of the Photon Emission Rate and Spectral Properties as Function of the Q-Factor

In the original CP-SFWM proposal using an optical fiber [66], the fiber length was the primary parameter controlling the photon-pair properties. In contrast, for our microresonator based photon source, the Airy functions play a significant role in the computation of the JSI (see Equations 3.33, 3.50), making the Q-factor the key parameter that determines the emission rate, bandwidth, and purity for a fixed cavity length. Figure 4.11 presents the results of an exploratory study we conducted to characterize how the photon source properties vary with different Q-factor values. In the simulations we used some reported values for silicon nitride ring-resonators: $Q = 1.3 \times 10^4$ [129], $Q = 4 \times 10^4$, $Q = 4.6 \times 10^5$ [130], $Q = 1.04 \times 10^6$ [46] and $Q = 1.4 \times 10^6$ [121]. Figure 4.11 a) shows that the photon emission rate increases with the Q-factor, whereas Figure 4.11 b) reveals a significant reduction in bandwidth, reaching the MHz scale. Both parameters asymptotically converge to values primarily dictated by the resonator length. Additionally, the purity was calculated for each Q-factor, consistently yielding a value

of $P = 1$, even at the lowest Q-factor. This outcome can be attributed to the broad bandwidth of the pulsed laser, which exceeds the cavity resonance width.

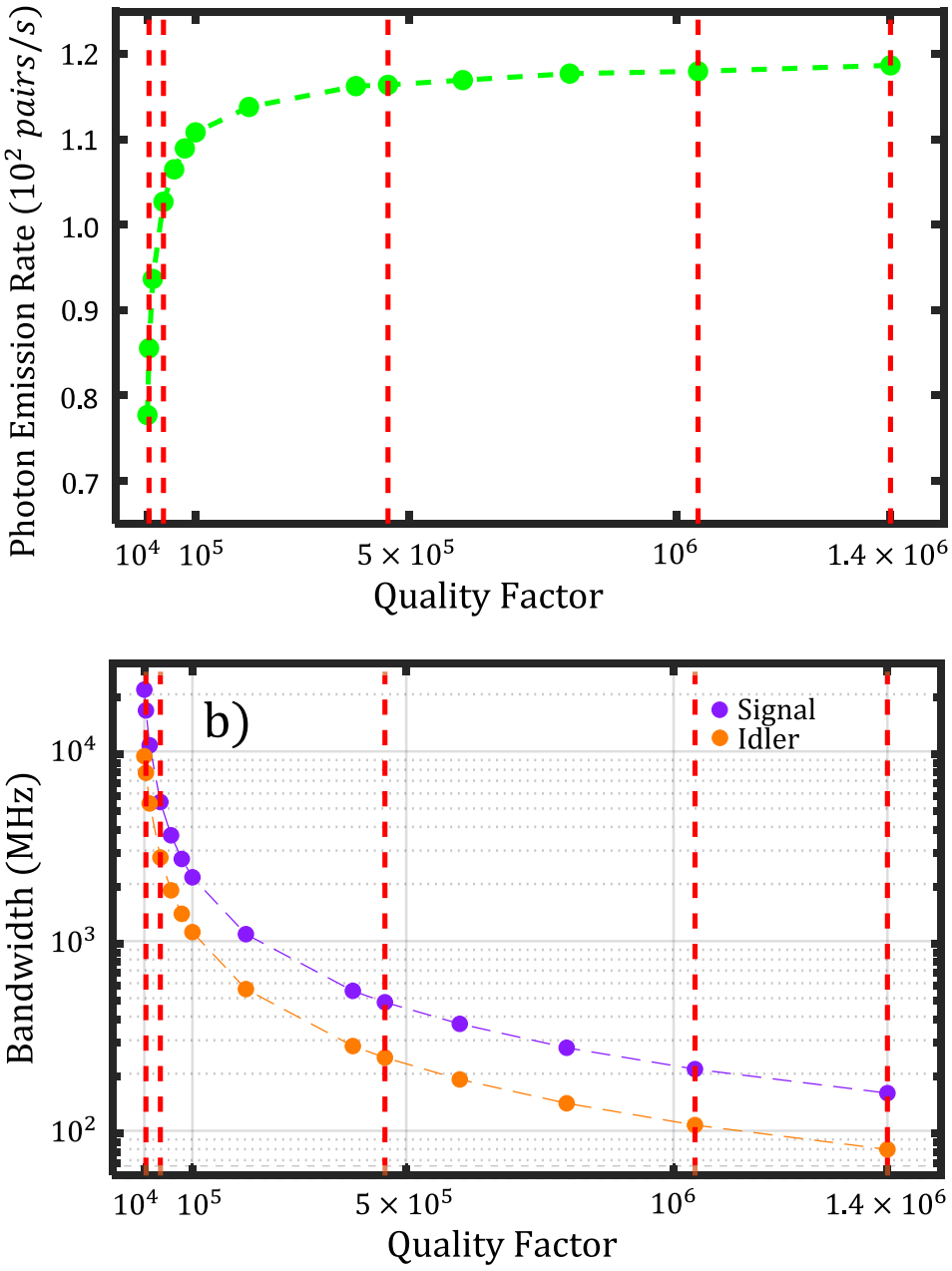

Fig. 4.11 Q-factor dependence of the characteristics of the photon-pairs produced with our source based on CP-SFWM in a ring resonator. (a) Photon emission rate. (b) Bandwidth of the signal and idler photons. The vertical lines corresponds to reported values in literature for silicon nitride ring resonators. In graph b) we use a logarithmic scale in the y-axis.

4.6 Fabrication and Characterization of a Chip-Integrated Microring Resonator

In this section, we present the characterization results of the quality factors of a chip developed in collaboration with Mauricio Robles and Dr. Rafael Salas from the University of Technology of Troyes (UTT), France, and Dr. Samuel Durán from Leibniz University, Hannover, Germany.

The sample of the chip consists of a 500 nm thick stoichiometric Si_3N_4 layer deposited on a 2 μm of SiO_2 thick layer, which is placed on top of a Si substrate. The device was quickly designed without an optimization process to take advantage of the opportunity to fabricate it alongside other devices in a fabrication round within this sample and to characterize it, obtaining preliminary results on its performance at the wavelengths of interest. We designed the microring resonator structures using Python library GDS Helpers [131], an open-source software tool for creating photonic circuit layouts. Figure 4.12 a) shows the final design of the device. We provided the files of the designed chip to Mauricio Robles and Dr. Rafael Salas. They fabricated it using electron beam lithography and reactive ion etching techniques at UTT. A detailed description of the complete fabrication process can be found in [132]. Figure 4.12 b) shows a microscope image of the resonator during operation, its geometric parameters are $h = 500\ nm,\ w = 800\ nm,\ R = 154\ \mu m,\ g_{s,i} = 400\ nm$.

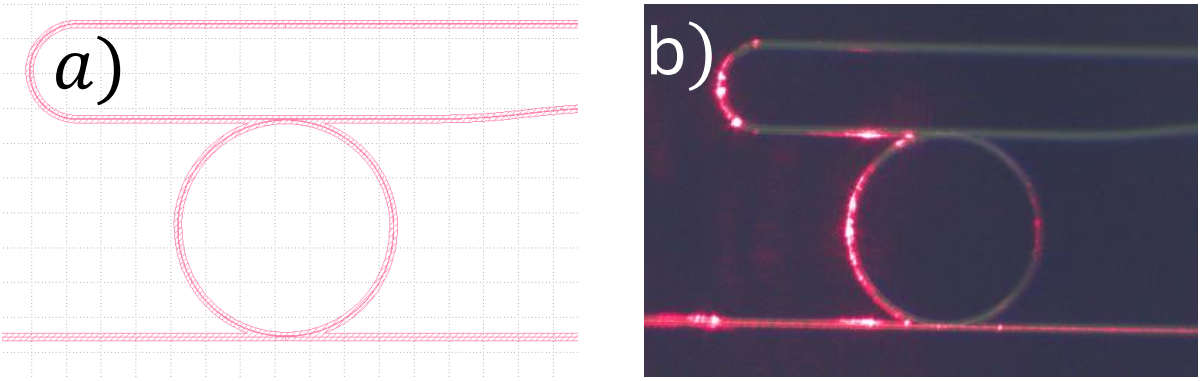

Fig. 4.12 a) GDS of the final device. b) Microscope image in which it is shown the ring resonator during characterization measurements. The red beam is a visible laser used to couple the optical fibers to the chip.

The characterization was carried out by Dr. Samuel Durán at Leibniz University. During the characterization process, the chip was placed on a temperature-controlled platform to maintain a stable temperature of 26.5°*C*. An Erbium Doped Fiber Amplifier (EDFA) was used as an Amplified Spontaneous Emission (ASE) source of broadband spectrum. Coupling and decoupling of the laser were performed using fiber lenses, and the beams were analyzed with an Optical Spectrum Analyzer. Dr. Samuel provided us with the raw transmission and drop spectra data, which we subsequently analyzed. In Figure 4.13, we present the transmission and drop spectra around 1550 nm. The transmission is measured at the output of the pump waveguide, while the drop is measured at the output of the other waveguide, where no pump is injected.

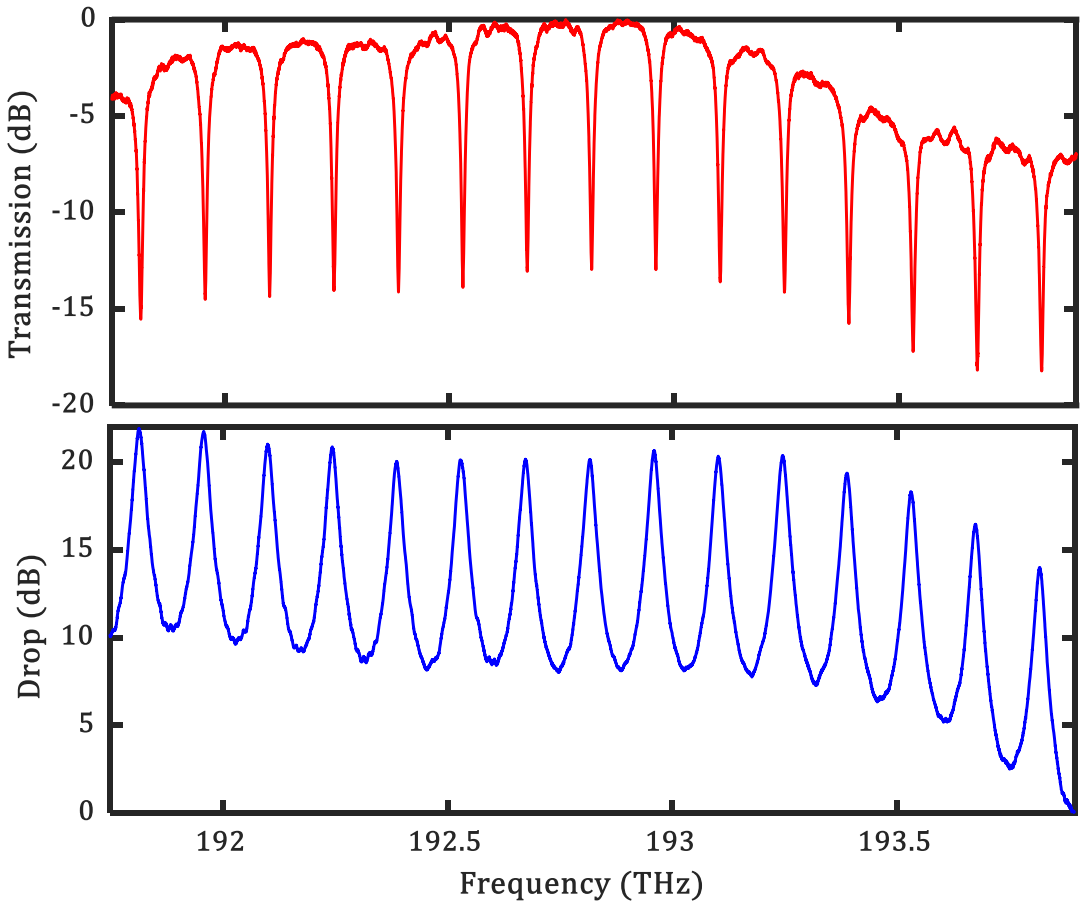

Fig. 4.13 Measured spectra of a) the transmission channel and b) the drop channel.

We identified the resonance closest to 1550 nm in both the transmission and drop spectra and fitted a Lorentzian function to the data to extract the bandwidths. Figure 4.14 shows the normalized resonances. We obtained bandwidths of 23.74 GHz and 21.40 GHz for the transmission and drop resonances, respectively. Their corresponding quality factors, computed using equation (4.7), are 8.15×10^3 and 9.04×10^3. As we mentioned in Section 4.5, characterization results indicate that even with a quality factor of this order, a pure state is achieved. However, a higher value is necessary to improve the emission rate and the bandwidths of photons.

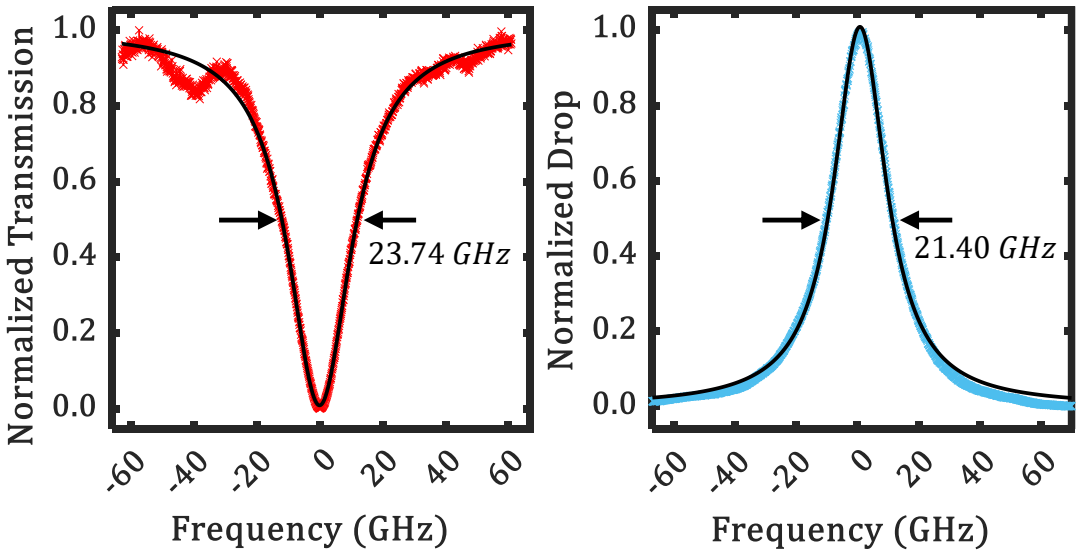

Fig. 4.14 Normalized resonances at 1550 *nm* of the a) transmission and b) drop spectrum.

We simulated this ring resonator using its geometrical parameters. The quality factors obtained using ANSYS Lumerical were $Q_i = 1.36 \times 10^6$, $Q_s = 3.48 \times 10^6$, approximately half of those of the optimized device ($Q_i = 2.28 \times 10^6$, $Q_s = 8.92 \times 10^6$). This outcome was expected because the geometrical parameters of this resonator were not optimized. Experimentally, the measured quality factor Q_i is approximately two orders of magnitude lower than the simulated value, likely due to intrinsic cavity losses caused by fabrication defects, which further degrade performance. However, with the measured quality factors, a purity of one is achievable according to the simulations, and a good photon emission rate of $N_p = 99.89$ pairs/s is expected. Future work will focus on improving the fabrication process to achieve higher quality factors.

Chapter 5

Conclusions

We presented the design of an integrated photon-pair source based on cavity-enhanced CP-SFWM, utilizing a mixed-pump scheme in a Si_3N_4 microring resonator with an add-drop configuration to generate photon pairs at 800 nm and 1550 nm. In this scheme, phase matching is inherently satisfied for photons at the same wavelengths as the pumps, eliminating the need for dispersion engineering. For the simulations, pump 1 was modeled as a pulsed laser centered at $\lambda_s = 800$ nm, while pump 2 was a CW laser centered at $\lambda_i = 1550$ nm.

The design of the device required an extensive optimization of the geometrical parameters, focusing on three key objectives:

- Maximizing the photon-pair emission rate by carefully selecting the waveguide's transverse dimensions.
- Identifying a resonator radius that satifies the resonance conditions for the signal and idler photon wavelengths, thereby ensuring the cavity-enhanced effect.
- Optimizing the coupling gaps between the bus waveguides for pumps 1 and 2 and the ring resonator to achieve the highest possible Q-factor.

The optimized design parameters for the photon source include a waveguide cross-section with a height of $h = 430$ nm and a width of $w = 794$ nm, a ring radius of $R = 156.34\ \mu m$, and

coupling gaps of 590 nm and 580 nm for the bus waveguides of pumps 1 and 2, respectively. These parameters align with reported values for Si_3N_4 chip-integrated ring resonators, making the proposed device feasible for implementation. Some of these values in the format (h, w, R, g) are: (450 nm, 1000 nm, 60 μm, 600 nm) [129], (500 nm, 1200 nm, 25 μm, 200 nm) [46], (500 nm, 200 nm, 300 μm, —) [121].

We analyzed the performance of the photon source through simulations, obtaining bandwidths for the signal and idler photons of $\Delta\nu_s = 157.9$ MHz and $\Delta\nu_i = 79.7$ MHz, respectively, assuming the highest reported Q-factor of $Q = 1.4 \times 10^6$ for a silicon nitride microring resonator. The source achieved an emission rate of $N_p = 118.70$ pairs/s. Additionally, we performed a numerical Schmidt decomposition of the JSI using SVD and demonstrated that the generated photon pairs exhibit a purity of $P = 1$, corresponding to a spectrally separable quantum state, a very important feature for implementation of quantum protocols.

We conducted an exploratory study by varying the Q-factor, underscoring its critical role as a control parameter that directly influences the emission rate of the integrated photon source and its spectral properties, including bandwidth and purity. Additionally, we compared our results with the original proposal and demonstrated that a chip-integrated source using a microring resonator overcomes the major limitation of requiring long interaction lengths in fiber-based implementations.

With the results we obtained, we demonstrated the advantages of CP-SFWM for implementing chip-integrated photon sources, highlighting three key benefits:

- It eliminates the need for dispersion engineering, as the phase-matching condition is inherently satisfied.
- Selecting a suitable ring resonator radius requires optimizing only two resonances instead of three, as in the co-propagating scheme, simplifying the design process.
- Spectrally pure photon pairs can be easily achieved by using a ring resonator with a reasonable quality factor ($Q \sim 10^4$).

These advantages make the scheme highly adaptable, requiring only lasers emitting at the desired wavelengths and compatible detectors. Such flexibility establishes our approach as a robust framework for designing tailored integrated photon-pair sources.

As mentioned at the beginning of Chapter 4, the choice of wavelengths $\lambda_s = 800$ nm, $\lambda = 1550$ nm was based on the availability of lasers at these wavelengths in our facilities. These wavelengths were not selected for a specific application, but rather to demonstrate the feasibility of implementing an integrated photon source based on CP-SFWM, with a view toward a future fabrication of the source. Despite this, our photon source could be adapted to make it suitable for applications in quantum memories based on erbium ions, since the wavelength for this application is 1536.48 nm [128], a very close value to the 1550 nm used in our simulations. We can confidently assert that the bandwidth of photons produced at this wavelength would be approximately the bandwidth we obtained (79.7 MHz) using a microring resonator of $Q = 1.4 \times 10^6$, which satisfies the requirement of being narrower than the maximum acceptable value (≈ 185 MHz)) for the efficient implementation of the protocol.

We reported the characterization of a ring resonator at $\lambda = 1550$ nm, developed in collaboration with colleagues from UTT and Leibniz University, and its corresponding simulation. The measured Q-factor values, $Q_i = 8.15 \times 10^3$, 9.04×10^3, were lower than those expected from the simulations ($Q_i = 1.36 \times 10^6$), likely due to intrinsic losses in the cavity caused by fabrication defects. Nevertheless, these values are sufficient to generate photons in a pure state. Addressing the fabrication issues will be critical for improving performance in future implementations.

Future work will involve fabricating the designed photon source using electron beam lithography at UTT, with a focus on improving the fabrication process of the photonic circuits to minimize losses caused by nonuniformity of the waveguides and surface roughness. Subsequently, the spectral properties and emission rates of both photon sources will be characterized at the Center for Research in Optics in León, Mexico. Additionally, in future implementations, we could expand the design of photon sources using this scheme by incorporating materials

such as SiC and AlGaAs, two alternatives with interesting optical properties, including high linear and nonlinear refractive indices, which enable better integration and enhance the photon emission rate.

References

[1] A. Einstein, B. Podolsky, and N. Rosen. Can quantum-mechanical description of physical reality be considered complete? *Phys. Rev.*, 47:777–780, May 1935.

[2] Erwin Schrödinger. The present status of quantum mechanics. *Die Naturwissenschaften*, 23(48):1–26, 1935.

[3] Max Planck. On the law of the energy distribution in the normal spectrum. *Ann. Phys*, 4(553):1–11, 1901.

[4] R. A. Millikan. A direct photoelectric determination of planck's "h". *Phys. Rev.*, 7:355–388, Mar 1916.

[5] C. Davisson and Germer L. H. The scattering of electrons by a single crystal of nickel. *Nature*, 119:558–560, 1927.

[6] Steve K Lamoreaux. A review of the experimental tests of quantum mechanics. *International Journal of Modern Physics A*, 7(27):6691–6762, 1992.

[7] Peter Shadbolt, Jonathan CF Mathews, Anthony Laing, and Jeremy L O'brien. Testing foundations of quantum mechanics with photons. *Nature Physics*, 10(4):278–286, 2014.

[8] T. H. Maiman. Stimulated optical radiation in ruby. *Nature*, 187(4736):493–494, 1960.

[9] P. A. Franken, A. E. Hill, C. W. Peters, and G. Weinreich. Generation of optical harmonics. *Phys. Rev. Lett.*, 7:118–119, Aug 1961.

[10] S. E. Harris, M. K. Oshman, and R. L. Byer. Observation of tunable optical parametric fluorescence. *Phys. Rev. Lett.*, 18:732–734, May 1967.

[11] J. D. Franson. Bell inequality for position and time. *Phys. Rev. Lett.*, 62:2205–2208, May 1989.

[12] Z. Y. Ou, X. Y. Zou, L. J. Wang, and L. Mandel. Observation of nonlocal interference in separated photon channels. *Phys. Rev. Lett.*, 65:321–324, Jul 1990.

[13] Alain Aspect, Philippe Grangier, and Gérard Roger. Experimental realization of einstein-podolsky-rosen-bohm gedankenexperiment: A new violation of bell's inequalities. *Phys. Rev. Lett.*, 49:91–94, Jul 1982.

[14] C. K. Hong, Z. Y. Ou, and L. Mandel. Measurement of subpicosecond time intervals between two photons by interference. *Phys. Rev. Lett.*, 59:2044–2046, Nov 1987.

[15] Dik Bouwmeester, Jian-Wei Pan, Klaus Mattle, Manfred Eibl, Harald Weinfurter, and Anton Zeilinger. Experimental quantum teleportation. *Nature*, 390:575–579, 1997.

[16] H. de Riedmatten, I. Marcikic, W. Tittel, H. Zbinden, and N. Gisin. Quantum interference with photon pairs created in spatially separated sources. *Phys. Rev. A*, 67:022301, Feb 2003.

[17] S. R. Friberg, S. Machida, M. J. Werner, A. Levanon, and Takaaki Mukai. Observation of optical soliton photon-number squeezing. *Phys. Rev. Lett.*, 77:3775–3778, Oct 1996.

[18] Charles H. Bennett and Gilles Brassard. Quantum cryptography: Public key distribution and coin tossing. *Theoretical Computer Science*, 560:7–11, 2014.

[19] Xu Liu, Xin Yao, Heqing Wang, Hao Li, Zhen Wang, Lixing You, Yidong Huang, and Wei Zhang. Energy-time entanglement-based dispersive optics quantum key distribution over optical fibers of 20 km. *Applied Physics Letters*, 114(14):141104, 04 2019.

[20] Emanuel Knill, Raymond Laflamme, and Gerard J. Milburn. A scheme for efficient quantum computation with linear optics. *Nature*, 409(6816):46–52, 2001.

[21] Jeremy L O'brien. Optical quantum computing. *Science*, 318(5856):1567–1570, 2007.

[22] J. et. al. Aasi. Enhancing the sensitivity of the ligo gravitational wave detector by using squeezed states of light. *Nature Photonics*, 7:613–619, 2013.

[23] Weihong Luo, Chao Wu, Yuxing Du, Chang Zhao, Miaomiao Yu, Pingyu Zhu, Kaikai Zhang, and Ping Xu. On-chip quantum noon state sensing for temperature and humidity. *Chinese Physics B*, 33(10):100305, sep 2024.

[24] Zhiliang Yuan, Beata E. Kardynal, R. Mark Stevenson, Andrew J. Shields, Charlene J. Lobo, Ken Cooper, Neil S. Beattie, David A. Ritchie, and Michael Pepper. Electrically driven single-photon source. *Science*, 295(5552):102–105, 2002.

[25] Satoshi Kako, Charles Santori, Katsuyuki Hoshino, Stephan Götzinger, Yoshihisa Yamamoto, and Yasuhiko Arakawa. A gallium nitride single-photon source operating at 200 k. *Nature Materials*, 5(11):887–892, November 2006.

[26] Xing Ding, Yu He, Z.-C. Duan, Niels Gregersen, M.-C. Chen, S. Unsleber, S. Maier, Christian Schneider, Martin Kamp, Sven Höfling, Chao-Yang Lu, and Jian-Wei Pan. On-demand single photons with high extraction efficiency and near-unity indistinguishability from a resonantly driven quantum dot in a micropillar. *Phys. Rev. Lett.*, 116:020401, Jan 2016.

[27] D B Higginbottom, L Slodička, G Araneda, L Lachman, R Filip, M Hennrich, and R Blatt. Pure single photons from a trapped atom source. *New Journal of Physics*, 18(9):093038, sep 2016.

[28] K. H. Madsen, S. Ates, J. Liu, A. Javadi, S. M. Albrecht, I. Yeo, S. Stobbe, and P. Lodahl. Efficient out-coupling of high-purity single photons from a coherent quantum dot in a photonic-crystal cavity. *Phys. Rev. B*, 90:155303, Oct 2014.

[29] Brian J. Smith, P. Mahou, Offir Cohen, J. S. Lundeen, and I. A. Walmsley. Photon pair generation in birefringent optical fibers. *Opt. Express*, 17(26):23589–23602, Dec 2009.

[30] J. G. Rarity, J. Fulconis, J. Duligall, W. J. Wadsworth, and P. St. J. Russell. Photonic crystal fiber source of correlated photon pairs. *Opt. Express*, 13(2):534–544, Jan 2005.

[31] Martin Cordier, Philippe Delaye, Frédéric Gérôme, Fetah Benabid, and Isabelle Zaquine. Raman-free fibered photon-pair source. *Scientific Reports*, 10:1650, 2020.

[32] Offir Cohen, Jeff S. Lundeen, Brian J. Smith, Graciana Puentes, Peter J. Mosley, and Ian A. Walmsley. Tailored photon-pair generation in optical fibers. *Phys. Rev. Lett.*, 102:123603, Mar 2009.

[33] A. A. Shukhin, J. Keloth, K. Hakuta, and A. A. Kalachev. Heralded single-photon and correlated-photon-pair generation via spontaneous four-wave mixing in tapered optical fibers. *Phys. Rev. A*, 101:053822, May 2020.

[34] Karina Garay-Palmett, Alfred B. U'Ren, and Raúl Rangel-Rojo. Conversion efficiency in the process of copolarized spontaneous four-wave mixing. *Phys. Rev. A*, 82:043809, Oct 2010.

[35] Evan Meyer-Scott, Nicola Montaut, Johannes Tiedau, Linda Sansoni, Harald Herrmann, Tim J. Bartley, and Christine Silberhorn. Limits on the heralding efficiencies and spectral purities of spectrally filtered single photons from photon-pair sources. *Phys. Rev. A*, 95:061803, Jun 2017.

[36] W. P. Grice, A. B. U'Ren, and I. A. Walmsley. Eliminating frequency and space-time correlations in multiphoton states. *Phys. Rev. A*, 64:063815, Nov 2001.

[37] Bin Fang, Offir Cohen, Jamy B. Moreno, and Virginia O. Lorenz. State engineering of photon pairs produced through dual-pump spontaneous four-wave mixing. *Opt. Express*, 21(3):2707–2717, Feb 2013.

[38] K. Garay-Palmett, H. J. McGuinness, Offir Cohen, J. S. Lundeen, R. Rangel-Rojo, A. B. U'Ren, M. G. Raymer, C. J. McKinstrie, S. Radic, and I. A. Walmsley. Photon pair-state preparation with tailored spectral properties by spontaneous four-wave mixing in photonic-crystal fiber. *Opt. Express*, 15(22):14870–14886, Oct 2007.

[39] C. J. Xin, Jatadhari Mishra, Changchen Chen, Di Zhu, Amirhassan Shams-Ansari, Carsten Langrock, Neil Sinclair, Franco N. C. Wong, M. M. Fejer, and Marko Lončar. Spectrally separable photon-pair generation in dispersion engineered thin-film lithium niobate. *Opt. Lett.*, 47(11):2830–2833, Jun 2022.

[40] Hatam Mahmudlu, Stuart May, Alí Angulo, Marc Sorel, and Michael Kues. Algaas-on-insulator waveguide for highly efficient photon-pair generation via spontaneous four-wave mixing. *Opt. Lett.*, 46(5):1061–1064, Mar 2021.

[41] Trevor J. Steiner, Joshua E. Castro, Lin Chang, Quynh Dang, Weiqiang Xie, Justin Norman, John E. Bowers, and Galan Moody. Ultrabright entangled-photon-pair generation from an AlGaAs-on-insulator microring resonator. *PRX Quantum*, 2:010337, Mar 2021.

[42] Rakesh Ranjan Kumar, Marina Raevskaia, Vadim Pogoretskii, Yuqing Jiao, and Hon Ki Tsang. Entangled photon pair generation from an inp membrane micro-ring resonator. *Applied Physics Letters*, 114(2):021104, 01 2019.

[43] Kai Guo, Erik N. Christensen, Jesper B. Christensen, Jacob G. Koefoed, Davide Bacco, Yunhong Ding, Haiyan Ou, and Karsten Rottwitt. High coincidence-to-accidental ratio continuous-wave photon-pair generation in a grating-coupled silicon strip waveguide. *Applied Physics Express*, 10(6):062801, may 2017.

[44] Chaoxuan Ma, Xiaoxi Wang, Vikas Anant, Andrew D. Beyer, Matthew D. Shaw, and Shayan Mookherjea. Silicon photonic entangled photon-pair and heralded single photon generation with car > 12,000 and g(2)(0) < 0.006. *Opt. Express*, 25(26):32995–33006, Dec 2017.

[45] Xiang Zhang, Yanbing Zhang, Chunle Xiong, and Benjamin J Eggleton. Correlated photon pair generation in low-loss double-stripe silicon nitride waveguides. *Journal of Optics*, 18(7):074016, jun 2016.

[46] Xiyuan Lu, Qing Li, Daron A Westly, Gregory Moille, Anshuman Singh, Vikas Anant, and Kartik Srinivasan. Chip-integrated visible–telecom entangled photon pair source for quantum communication. *Nature physics*, 15(4):373–381, 2019.

[47] David J Moss, Roberto Morandotti, Alexander L Gaeta, and Michal Lipson. New cmos-compatible platforms based on silicon nitride and hydex for nonlinear optics. *Nature photonics*, 7(8):597–607, 2013.

[48] Justin B. Spring, Benjamin J. Metcalf, Peter C. Humphreys, W. Steven Kolthammer, Xian-Min Jin, Marco Barbieri, Animesh Datta, Nicholas Thomas-Peter, Nathan K. Langford, Dmytro Kundys, James C. Gates, Brian J. Smith, Peter G. R. Smith, and Ian A. Walmsley. Boson sampling on a photonic chip. *Science*, 339(6121):798–801, 2013.

[49] Benjamin J. Metcalf, Justin B. Spring, Peter C. Humphreys, Nicholas Thomas-Peter, Marco Barbieri, W. Steven Kolthammer, Xian-Min Jin, Nathan K. Langford, Dmytro Kundys, James C. Gates, Brian J. Smith, Peter G. R. Smith, and Ian A. Walmsley. Quantum teleportation on a photonic chip. *Nature Photonics*, 8(10):770–774, 2014.

[50] Justin B. Spring, Patrick S. Salter, Benjamin J. Metcalf, Peter C. Humphreys, Merritt Moore, Nicholas Thomas-Peter, Marco Barbieri, Xian-Min Jin, Nathan K. Langford, W. Steven Kolthammer, Martin J. Booth, and Ian A. Walmsley. On-chip low loss heralded source of pure single photons. *Opt. Express*, 21(11):13522–13532, Jun 2013.

[51] Justin B. Spring, Paolo L. Mennea, Benjamin J. Metcalf, Peter C. Humphreys, James C. Gates, Helen L. Rogers, Christoph Söller, Brian J. Smith, W. Steven Kolthammer, Peter G. R. Smith, and Ian A. Walmsley. Chip-based array of near-identical, pure, heralded single-photon sources. *Optica*, 4(1):90–96, Jan 2017.

[52] S. Paesani, M. Borghi, S. Signorini, A. Maïnos, L. Pavesi, and A. Laing. Near-ideal spontaneous photon sources in silicon quantum photonics. *Nature Communications*, 11(1):2505, May 2020.

[53] Mingfei Ding, Ming Zhang, Shihan Hong, Yi Zhao, Long Zhang, Yi Wang, Haitao Chen, Zejie Yu, Shiming Gao, and Daoxin Dai. High-efficiency four-wave mixing in low-loss silicon photonic spiral waveguides beyond the singlemode regime. *Opt. Express*, 30(10):16362–16373, May 2022.

[54] S. Clemmen, K. Phan Huy, W. Bogaerts, R. G. Baets, Ph. Emplit, and S. Massar. Continuous wave photon pair generation in silicon-on-insulator waveguides and ring resonators. *Opt. Express*, 17(19):16558–16570, Sep 2009.

[55] Jelena V Rakonjac, Giacomo Corrielli, Dario Lago-Rivera, Alessandro Seri, Margherita Mazzera, Samuele Grandi, Roberto Osellame, and Hugues de Riedmatten. Storage and analysis of light-matter entanglement in a fiber-integrated system. *Science Advances*, 8(27):eabn3919, 2022.

[56] M Nicolle, JN Becker, C Weinzetl, IA Walmsley, and PM Ledingham. Gigahertz-bandwidth optical memory in pr 3+: Y 2 sio 5. *Optics Letters*, 46(12):2948–2951, 2021.

[57] Erhan Saglamyurek, Jeongwan Jin, Varun B Verma, Matthew D Shaw, Francesco Marsili, Sae Woo Nam, Daniel Oblak, and Wolfgang Tittel. Quantum storage of entangled telecom-wavelength photons in an erbium-doped optical fibre. *Nature Photonics*, 9(2):83–87, 2015.

[58] Daniel Llewellyn, Yunhong Ding, Imad I Faruque, Stefano Paesani, Davide Bacco, Raffaele Santagati, Yan-Jun Qian, Yan Li, Yun-Feng Xiao, Marcus Huber, et al. Chip-to-chip quantum teleportation and multi-photon entanglement in silicon. *Nature Physics*, 16(2):148–153, 2020.

[59] Patrick Yard, Alex E Jones, Stefano Paesani, Alexandre Maïnos, Jacob FF Bulmer, and Anthony Laing. On-chip quantum information processing with distinguishable photons. *Physical Review Letters*, 132(15):150602, 2024.

[60] PP Yupapin. Generalized quantum key distribution via micro ring resonator for mobile telephone networks. *Optik*, 121(5):422–425, 2010.

[61] Noemi Tagliavacche, Massimo Borghi, Giulia Guarda, Domenico Ribezzo, Marco Liscidini, Davide Bacco, Matteo Galli, and Daniele Bajoni. Frequency-bin entanglement-based quantum key distribution. *arXiv preprint arXiv:2411.07884*, 2024.

[62] K Sugiura, Z Yin, R Okamoto, L Zhang, L Kang, J Chen, P Wu, ST Chu, BE Little, and S Takeuchi. Broadband generation of photon-pairs from a cmos compatible device. *Applied Physics Letters*, 116(22), 2020.

[63] Zhenghao Yin, Kenta Sugiura, Hideaki Takashima, Ryo Okamoto, Feng Qiu, Shiyoshi Yokoyama, and Shigeki Takeuchi. Frequency correlated photon generation at telecom band using silicon nitride ring cavities. *Optics Express*, 29(4):4821–4829, 2021.

[64] Kamal Kishor Choure, Ankur Saharia, Nitesh Mudgal, Rahul Pandey, Manisha Prajapat, Ravi Kumar Maddila, Manish Tiwari, and Ghanshyam Singh. Implementation of all-optical single qubit gates using si3n4 based micro ring resonator. *Optics & Laser Technology*, 170:110263, 2024.

[65] Davide Grassani, Stefano Azzini, Marco Liscidini, Matteo Galli, Michael J Strain, Marc Sorel, JE Sipe, and Daniele Bajoni. Micrometer-scale integrated silicon source of time-energy entangled photons. *Optica*, 2(2):88–94, 2015.

[66] Jorge Monroy-Ruz, Karina Garay-Palmett, and Alfred B U'Ren. Counter-propagating spontaneous four wave mixing: photon-pair factorability and ultra-narrowband single photons. *New Journal of Physics*, 18(10):103026, oct 2016.

[67] Alessandra Gatti and Enrico Brambilla. Heralding pure single photons: A comparison between counterpropagating and copropagating twin photons. *Physical Review A*, 97(1):013838, 2018.

[68] Wu-Hao Cai, Bei Wei, Shun Wang, and Rui-Bo Jin. Counter-propagating spectrally uncorrelated biphotons at 1550 nm generated from periodically poled mtioxo 4 (m= k, rb, cs; x= p, as). *JOSA B*, 37(10):3048–3054, 2020.

[69] Sina Saravi, Yu Zhang, Xiao Chen, Mina Afsharnia, Frank Setzpfandt, and Thomas Pertsch. Generation of counterpropagating and spectrally uncorrelated photon-pair states by spontaneous four-wave mixing in photonic crystal waveguides. *Frontiers in Photonics*, 3:953105, 2022.

[70] Kai-Hong Luo, Vahid Ansari, Marcello Massaro, Matteo Santandrea, Christof Eigner, Raimund Ricken, Harald Herrmann, and Christine Silberhorn. Counter-propagating photon pair generation in a nonlinear waveguide. *Optics Express*, 28(3):3215–3225, 2020.

[71] Yi-Chen Liu, Dong-Jie Guo, Kun-Qian Ren, Ran Yang, Minghao Shang, Wei Zhou, Xinhui Li, Chang-Wei Sun, Ping Xu, Zhenda Xie, et al. Observation of frequency-uncorrelated photon pairs generated by counter-propagating spontaneous parametric down-conversion. *Scientific Reports*, 11(1):12628, 2021.

[72] Paulina S Kuo, Dileep V Reddy, Varun Verma, Sae Woo Nam, Andrius Zukauskas, and Carlota Canalias. Photon-pair production and frequency translation using backward-wave spontaneous parametric downconversion. *Optica Quantum*, 1(2):43–48, 2023.

[73] J. S. S. Durán Gómez, R. Ramírez Alarcón, M. Gómez Robles, P. M. C. Tavares Ramírez, G. J. Rodríguez Becerra, E. Ortíz-Ricardo, and R. Salas-Montiel. Integrated photon pair source based on a silicon nitride micro-ring resonator for quantum memories. *Opt. Lett.*, 49(7):1860–1863, Apr 2024.

[74] P. M. C. Tavares Ramírez, J. S. S. Durán Gómez, G. J. Rodríguez Becerra, R. Ramírez-Alarcón, M. Gómez Robles, and R. Salas-Montiel. Integrated photon pairs source in silicon carbide based on micro-ring resonators for quantum storage at telecom wavelengths. *Scientific Reports*, 14(1):17755, August 2024.

[75] J. M. Chavez Boggio, D. Bodenmüller, T. Fremberg, R. Haynes, M. M. Roth, R. Eisermann, M. Lisker, L. Zimmermann, and M. Böhm. Dispersion engineered silicon nitride waveguides by geometrical and refractive-index optimization. *J. Opt. Soc. Am. B*, 31(11):2846–2857, Nov 2014.

[76] David Thomson, Aaron Zilkie, John E Bowers, Tin Komljenovic, Graham T Reed, Laurent Vivien, Delphine Marris-Morini, Eric Cassan, Léopold Virot, Jean-Marc Fédéli, Jean-Michel Hartmann, Jens H Schmid, Dan-Xia Xu, Frédéric Boeuf, Peter O'Brien, Goran Z Mashanovich, and M Nedeljkovic. Roadmap on silicon photonics. *Journal of Optics*, 18(7):073003, jun 2016.

[77] Aleksandr Biberman, Michael J. Shaw, Erman Timurdogan, Jeremy B. Wright, and Michael R. Watts. Ultralow-loss silicon ring resonators. *Opt. Lett.*, 37(20):4236–4238, Oct 2012.

[78] Nahum Izhaky, Michael T. Morse, Sean Koehl, Oded Cohen, Doron Rubin, Assia Barkai, Gadi Sarid, Rami Cohen, and Mario J. Paniccia. Development of cmos-compatible integrated silicon photonics devices. *IEEE Journal of Selected Topics in Quantum Electronics*, 12(6):1688–1698, 2006.

[79] Richard Soref. Mid-infrared photonics in silicon and germanium. *Nature Photonics*, 4(8):495–497, August 2010.

[80] Xinzhu Sang, En-Kuang Tien, and Ozdal Boyraz. Applications of two photon absorption in silicon. *Journal of optoelectronics and advanced materials*, 11(1):15–25, 2009.

[81] Chao Xiang, Warren Jin, Joel Guo, Coleman Williams, Andrew M. Netherton, Lin Chang, Paul A. Morton, and John E. Bowers. Effects of nonlinear loss in high-q si ring resonators for narrow-linewidth iii-v/si heterogeneously integrated tunable lasers. *Opt. Express*, 28(14):19926–19936, Jul 2020.

[82] Clemens J. Krückel, Attila Fülöp, Zhichao Ye, Peter A. Andrekson, and Victor Torres-Company. Optical bandgap engineering in nonlinear silicon nitride waveguides. *Opt. Express*, 25(13):15370–15380, Jun 2017.

[83] D. T. H. Tan, K. Ikeda, P. C. Sun, and Y. Fainman. Group velocity dispersion and self phase modulation in silicon nitride waveguides. *Applied Physics Letters*, 96(6):061101, February 2010.

[84] Abdul Rahim, Eva Ryckeboer, Ananth Z. Subramanian, Stéphane Clemmen, Bart Kuyken, Ashim Dhakal, Ali Raza, Artur Hermans, Muhammad Muneeb, Sören Dhoore, Yanlu Li, Utsav Dave, Peter Bienstman, Nicolas Le Thomas, Günther Roelkens, Dries Van Thourhout, Philippe Helin, Simone Severi, Xavier Rottenberg, and Roel Baets. Expanding the silicon photonics portfolio with silicon nitride photonic integrated circuits. *Journal of Lightwave Technology*, 35(4):639–649, 2017.

[85] Xingchen Ji, Felippe A. S. Barbosa, Samantha P. Roberts, Avik Dutt, Jaime Cardenas, Yoshitomo Okawachi, Alex Bryant, Alexander L. Gaeta, and Michal Lipson. Ultra-low-loss on-chip resonators with sub-milliwatt parametric oscillation threshold. *Optica*, 4(6):619–624, Jun 2017.

[86] Junqiu Liu, Guanhao Huang, Rui Ning Wang, Jijun He, Arslan S. Raja, Tianyi Liu, Nils J. Engelsen, and Tobias J. Kippenberg. High-yield, wafer-scale fabrication of ultralow-loss, dispersion-engineered silicon nitride photonic circuits. *Nature Communications*, 12(1):2236, April 2021.

[87] K Garay-Palmett, Y Jeronimo-Moreno, and A B U'Ren. Theory of cavity-enhanced spontaneous four wave mixing. *Laser Physics*, 23(1):015201, nov 2012.

[88] Xiyuan Lu, Gregory Moille, Qing Li, Daron A. Westly, Anshuman Singh, Ashutosh Rao, Su-Peng Yu, Travis C. Briles, Scott B. Papp, and Kartik Srinivasan. Efficient telecom-to-visible spectral translation through ultralow power nonlinear nanophotonics. *Nature Photonics*, 13(9):593–601, 2019.

[89] Vijay, Shivani Sharma, Vivek Venkataraman, and Joyee Ghosh. Sin waveguides for ultra-broadband visible-telecom photon pairs. *Optical and Quantum Electronics*, 55(7):582, 2023.

[90] Vijay, Shivani Sharma, Joyee Ghosh, and Vivek Venkataraman. Spectrally pure visible-telecom photon pairs via dispersion-engineered Si_3n_4 waveguides. *Phys. Rev. Appl.*, 22:014070, Jul 2024.

[91] Fabian Beutel, Thomas Grottke, Martin A. Wolff, Carsten Schuck, and Wolfram H. P. Pernice. Cryo-compatible opto-mechanical low-voltage phase-modulator integrated with superconducting single-photon detectors. *Opt. Express*, 30(17):30066–30074, Aug 2022.

[92] Guozhen Liang, Heqing Huang, Aseema Mohanty, Min Chul Shin, Xingchen Ji, Michael Joseph Carter, Sajan Shrestha, Michal Lipson, and Nanfang Yu. Robust, efficient, micrometre-scale phase modulators at visible wavelengths. *Nature Photonics*, 15(12):908–913, 2021.

[93] Mateus Corato-Zanarella, Andres Gil-Molina, Xingchen Ji, Min Chul Shin, Aseema Mohanty, and Michal Lipson. Widely tunable and narrow-linewidth chip-scale lasers from near-ultraviolet to near-infrared wavelengths. *Nature Photonics*, 17(2):157–164, 2023.

[94] C. A. A. Franken, A. van Rees, L. V. Winkler, Y. Fan, D. Geskus, R. Dekker, D. H. Geuzebroek, C. Fallnich, P. J. M. van der Slot, and K.-J. Boller. Hybrid-integrated diode laser in the visible spectral range. *Opt. Lett.*, 46(19):4904–4907, Oct 2021.

[95] Raghi S El Shamy, Mohamed A Swillam, and Xun Li. Optimization of silicon nitride waveguide platform for on-chip virus detection. *Sensors*, 22(3):1152, 2022.

[96] Junchao Zhou, Diana Al Husseini, Junyan Li, Zhihai Lin, Svetlana Sukhishvili, Gerard L Coté, Ricardo Gutierrez-Osuna, and Pao Tai Lin. Detection of volatile organic compounds using mid-infrared silicon nitride waveguide sensors. *Scientific Reports*, 12(1):5572, 2022.

[97] Leimeng Zhuang, Chris GH Roeloffzen, Marcel Hoekman, Klaus-J Boller, and Arthur J Lowery. Programmable photonic signal processor chip for radiofrequency applications. *Optica*, 2(10):854–859, 2015.

[98] Xia Fengnian, Lidija Sekaric, and Yurii Vlasov. Ultracompact optical buffers on a silicon chip. *Nature Photonics*, 1(1):65–71, 2007.

[99] Tai Tsuchizawa, Koji Yamada, Hiroshi Fukuda, Toshifumi Watanabe, Shingo Uchiyama, and Seiichi Itabashi. Low-loss si wire waveguides and their application to thermooptic switches. *Japanese Journal of Applied Physics*, 45(8S):6658–6662, aug 2006.

[100] Xinglin Zeng, Yan Li, Qi Mo, Wei Li, Yongjie Tian, Zhijian Liu, and Jian Wu. Experimental investigation of lp11 mode to oam conversion in few mode-polarization maintaining fiber and the usage for all fiber oam generator. *IEEE Photonics Journal*, 8(4):1–7, 2016.

[101] Fedor Mitschke. *Fiber Optics Physics and Technology*. Springer, Germany, first edition, 2010.

[102] Dr. Manfred Hammer. Modes of circular multi-step index optical fibers. https://www.siio.eu/fims.html, 2024. Último acceso: 20 de noviembre de 2024.

[103] Heebner John, Grover Rohit, and A. Ibrahim Tarek. *Optical Microresonators*. Springer, United States of America, first edition, 2008.

[104] D. F. Walls and G. J. Milburn. *Quantum Optics*. Springer, Berlin, Germany, 2nd edition, 2008.

[105] Christopher Gerry and Peter Knight. *Introductory Quantum Optics*. Cambridge University Press, Cambridge, UK, 2005.

[106] John David Jackson. *Classical Electrodynamics*. Wiley, New York, NY, 3rd edition, 1998.

[107] Robert W. Boyd. *Nonlinear Optics*. Academic Press, Burlington, MA, 3rd edition, 2008.

[108] Kirankumar Rajshekhar Hiremath. *COUPLED MODE THEORY BASED MODELING AND ANALYSIS OF CIRCULAR OPTICAL MICRORESONATORS*. PhD thesis, University of Twente, Enschede, The Netherlands, 2005.

[109] M. Hammer, K. R. Hiremath, and R. Stoffer. Analytical approaches to the description of optical microresonator devices. *AIP Conference Proceedings*, 709(1):48–71, 2004.

[110] Nouredine Zettili. *Quantum Mechanics: Concepts and Applications*. Wiley, Chichester, UK, 2nd edition, 2009.

[111] Peter J Mosley, Jeff S Lundeen, Brian J Smith, and Ian A Walmsley. Conditional preparation of single photons using parametric downconversion: a recipe for purity. *New Journal of Physics*, 10(9):093011, 2008.

[112] Artur Ekert and Peter L. Knight. Entangled quantum systems and the schmidt decomposition. *American Journal of Physics*, 63(5):415–423, 05 1995.

[113] S. Parker, S. Bose, and M. B. Plenio. Entanglement quantification and purification in continuous-variable systems. *Phys. Rev. A*, 61:032305, Feb 2000.

[114] Kevin Zielnicki, Karina Garay-Palmett, Daniel Cruz-Delgado, Hector Cruz-Ramirez, Michael F. O'Boyle, Bin Fang, Virginia O. Lorenz, Alfred B. U'Ren, and Paul G. Kwiat. Joint spectral characterization of photon-pair sources. *Journal of Modern Optics*, 65(10):1141–1160, 2018.

[115] Francesco Martini and Alberto Politi. Four wave mixing in 3c sic ring resonators. *Applied Physics Letters*, 112(25):251110, 06 2018.

[116] Thor Labs. Pulsed lasers introduction to power and energy calculations. https://www.thorlabs.com/images/tabimages/Laser_Pulses_Power_Energy_Equations.pdf, 2024. Último acceso: 20 de noviembre de 2024.

[117] Arman B. Fallahkhair, Kai S. Li, and Thomas E. Murphy. Vector finite difference modesolver for anisotropic dielectric waveguides. *Journal of Lightwave Technology*, 26(11):1423–1431, 2008.

[118] I. H. Malitson. Interspecimen comparison of the refractive index of fused silica∗,†. *Journal of the Optical Society of America*, 55(10):1205–1209, Oct 1965.

[119] Kevin Luke, Yoshitomo Okawachi, Michael RE Lamont, Alexander L Gaeta, and Michal Lipson. Broadband mid-infrared frequency comb generation in a si 3 n 4 microresonator. *Optics letters*, 40(21):4823–4826, 2015.

[120] Govind P. Agrawal. *Nonlinear Fiber Optics*. Academic Press, San Diego, 3rd edition, 2001.

[121] Martin Sinclair, Kevin Gallacher, Marc Sorel, Joseph C. Bayley, Euan McBrearty, Ross W. Millar, Stefan Hild, and Douglas J. Paul Paul. 1.4 million Q factor Si_3N_4 micro-ring resonator at 780 nm wavelength for chip-scale atomic systems. *Opt. Express*, 28(3):4010–4020, 2020.

[122] Coherent. Chameleon ti:saphire lasers. https://www.coherent.com/content/dam/coherent/site/en/resources/datasheet/lasers/COHR_ChameleonVision_DS_0119_5.pdf.

[123] Newport. V. t. lasers. https://www.newport.com/p/TLB-6730.

[124] ANSYS-Lumerical. Ring resonator getting started - design and initial simulation. https://optics.ansys.com/hc/en-us/articles/360042800293-Ring-resonator-getting-started-Design-and-initial-simulation.

[125] ANSYS-Lumerical. Ring resonator using interconnect primitive elements. https://optics.ansys.com/hc/en-us/articles/360042323794-Ring-resonator-using-INTERCONNECT-primitive-elements.

[126] Durán Gómez Juan Samuel Sebastián. *INTEGRATED MICRORING RESONATORS FOR PHOTONIC QUANTUM TECHNOLOGIES*. PhD thesis, Centro de Investigaciones en Óptica A. C., León, Guanajuato, México, 2024.

[127] Richard L. Burden and J. Douglas Faires. *Numerical Analysis*. Brooks/Cole, Cengage Learning, Boston, MA, 9 edition, 2010.

[128] Ming-Hao Jiang, Wenyi Xue, Qian He, Yu-Yang An, Xiaodong Zheng, Wen-Jie Xu, Yu-Bo Xie, Yanqing Lu, Shining Zhu, and Xiao-Song Ma. Quantum storage of entangled photons at telecom wavelengths in a crystal. *Nature Communications*, 14(1):6995, 2023.

[129] I.N. Chuprina, P.P. An, E.G. Zubkova, V.V. Kovalyuk, A.A. Kalachev, and G.N. Gol'tsman. Optimisation of spontaneous four-wave mixing in a ring microcavity. *Quantum Electronics*, 47(10):887–891, 2017.

[130] Farid Samara, Anthony Martin, Claire Autebert, Maxim Karpov, Tobias J. Kippenberg, Hugo Zbinden, and Rob Thew. High-rate photon pairs and sequential time-bin entanglement with si3n4 microring resonators. *Optics Express*, 27(14):19309–19318, Jul 2019.

[131] Helge Gehring, Matthias Blaicher, Wladick Hartmann, and Wolfram HP Pernice. Python based open source design framework for integrated nanophotonic and superconducting circuitry with 2d-3d-hybrid integration. *OSA Continuum*, 2(11):3091–3101, 2019.

[132] Juan Samuel Sebastián Durán Gómez. Integrated nanophotonic waveguide lattices as photonic quantum simulators. Master's thesis, Centro de Investigaciones en Óptica A.C, 2019.